Towards Scanning Tunneling Microscopy in a Dry Dilution Refrigerator

Stallen, Martijn

Towards Scanning Tunneling Microscopy in a Dry Dilution Refrigerator

THESIS

submitted in partial fulfillment of the
requirements for the degree of

BACHELOR OF SCIENCE
in
PHYSICS

Author :	M. J. J. Stallen
Student ID :	s2966670
Supervisor :	Prof.dr.ir. T. H. Oosterkamp
	K. van Deelen MSc
Second corrector :	Prof.dr. J. M. van Ruitenbeek

Leiden, The Netherlands, July 7, 2023

Towards Scanning Tunneling Microscopy in a Dry Dilution Refrigerator

M. J. J. Stallen

Huygens-Kamerlingh Onnes Laboratory, Leiden University
P.O. Box 9500, 2300 RA Leiden, The Netherlands

July 7, 2023

Abstract

Scanning Tunneling Microscopy (STM) is a technique that allows its user to make scans of the surface topography of a sample. Via a capacitive approach, a tip is brought in close proximity to the sample, by which eventually a tunneling current is measured that is used to obtain a scan. It can be interesting to do STM experiments at extremely low temperatures (< 4 K), which can be done by placing an STM into a dilution refrigerator. It is difficult to do so in a dry dilution refrigerator, because of the pulse tube system that brings lots of mechanical vibrations. This research shows the performance of the newly developed 'PAN-motor' and 'linear cryo-walkers', two new types of motors for STM-approaches at extremely low temperatures. The cryo-walkers in particular have allowed for a full approach at millikelvin temperatures due to its low heat dissipation, whereas this approach normally has to be done above 4 K. By realizing dry dilution refrigerator STM, more research at millikelvin temperatures would be made possible, due to these dry dilution refrigerators being closed systems, allowing for time-unlimited measurements. This advancement could allow for experiments with low T_c superconductors, or shot noise experiments with the new Multi-LC circuit, that has shown to enable the measurement of shot noise with a total measuring time of $\tau \approx 98$ h.

Contents

Version of July 7, 2023– Created July 7, 2023 - 11:30

Version of July 7, 2023– Created July 7, 2023 - 11:30

Chapter 1

Introduction

In 1983, Gerd Binnig and Heinrich Rohrer had a paper published on their realization of Scanning Tunneling Microscopy (STM) [1], for which they would receive the Nobel Prize for Physics in 1986 [2]. This new, revolutionary technology would yield a new way of mapping surface topographies. Ever since its discovery, STM has been used in numerous fields [3–5] and is still a very active topic of research in physics [6–8].

Another field in which STM can be used, is the study of materials at extremely low temperatures (below 4 K). To reach these temperatures, an STM can be placed within a wet dilution refrigerator [9, 10] or, while less common, a dry dilution refrigerator [11]. Under these cryogenic conditions, it is possible to measure shot noise in an STM, which has previously been used to study the nature of charge transport in superconductors [7]. In the Oosterkamp Group at Leiden University, we aim to enable shot noise measurements at multiple frequencies in the MHz regime by use of the so-called 'Multi-LC' circuit, that uses a combination of LC-resonators and a SQUID. These measurements can in the future be achieved by working at millikelvin temperatures with an STM connected to the Multi-LC circuit.

For this project, the performance at sub-kelvin temperatures of two STM's is tested, differing from each other by the type of motor responsible for tip movement. The probehead STM (PH-STM) makes use of six slip-stick piezo actuators in a configuration called 'the PAN-motor', whereas the Basic STM uses newly designed 'linear cryo-walkers'. Both STM's have been developed by Leiden Probe Microscopy (LPM). To test these at extremely low temperatures, they were placed in the *Marshmallow* cryostat of the Oosterkamp Group. The *Marshmallow* is a dry dilution refrigerator, designed by Leiden Cryogenics, which has been customized to

have a great vibration isolation system (VIS). Early work on the VIS was presented by den Haan et al. in 2014 on the *Olaf* cryostat, and in more recent work the VIS in *Marshmallow* has allowed for MRFM measurements at a sub-femtonewton scale [12].

By achieving dry dilution fridge STM, a great new milestone would be reached. Firstly, dry dilution refrigerators lack the need for a constant input of cryogenic fluids, being a closed system, which is a clear advantage over wet dilution refrigerators, that do require such constant input. This requirement limits the time of experiments to the available amount of liquid He, whereas a dry dilution refrigerator could theoretically run forever. One disadvantage is the large amount of vibrational noise introduced by the pulse tube. The effects of these vibrations on experiments can be alleviated, by hanging the experiments on long, rigid springs.

Secondly, if the tested STM's show low enough heat dissipation, they could enable STM experiments at sub-100mK temperatures, which would allow for the study of extremely low temperature T_c superconductors like tungsten ($\sim$15mK) [13] and iridium ($\sim$112 mK) [14]. The aforementioned shot noise measurements would be easier under these conditions, as the amount of thermal noise is greatly reduced in comparison to other shot noise measurements at temperatures of 4 K and upwards [7]. Another example is the use of a superconducting STM-tip to perform Scanning Tunneling Spectroscopy (STS), which is greatly facilitated by the extremely low temperatures.

This thesis shall discuss the performed experiments and its implications. Whilst the performance of the PH-STM's slip-stick actuators has been tested at RT as well (Ch. 4), both the PH-STM and Basic STM were placed in a dilution refrigerator to test for their performance (Ch. 5 & 6). At extremely low temperatures, the capacitance of the piezoelectric elements in the motors can decrease drastically, possibly preventing all movement. This movement was tested for via performing capacitive approaches, as proposed by de Voogd et al. [15]. An attempt at making scans with both STM's has also been made (Ch. 4, 5 & 6). Finally, a study on the usability of the mentioned Multi-LC circuit for shot noise measurements has been performed (Ch. 7).

Chapter 2

Theory

Within this first chapter, theory relevant for the project shall be discussed. This includes some general considerations on the Scanning Tunneling Microscope (STM) - what conditions an STM-tip and sample should abide to, and theory regarding piezoelectric elements - followed by theory relevant to the STM-circuit. The chapter shall be rounded off with a short discussion on cryostats.

2.1 Scanning Tunneling Microscope

With the invention of STM, a new branch of microscopy took shape that focuses on the formation of images of surface structures using a physical scanning probe. In STM, a tip is brought very close (generally tens of micrometers) to a sample by use of a motor, after which a voltage is set on said sample. Due to the fact that the tip and sample are not in contact with each other, they form a finite potential well, causing a tunneling current to flow. Subsequently, the tunneling current is amplified (as the order of magnitude of the current is $\sim$1 nA) and converted to a voltage using an I/V-converter. The tunneling current can be related to the distance s between tip and sample, given a DC sample bias V_{bias}, through [16]

$$I_{TC} \propto V_{bias} \cdot e^{-2\kappa s} \tag{2.1}$$

where κ is a decay constant, that is dependent on the effective tunneling barrier height. After a tunneling current is measured, a feedback system is initiated to keep the current at a constant level, after which a piezoelectric tube scanner will perform a scan. Since the magnitude of the current is

related to the distance between tip and sample, relative distances can be mapped by use of the voltage that is sent to stay in constant current.

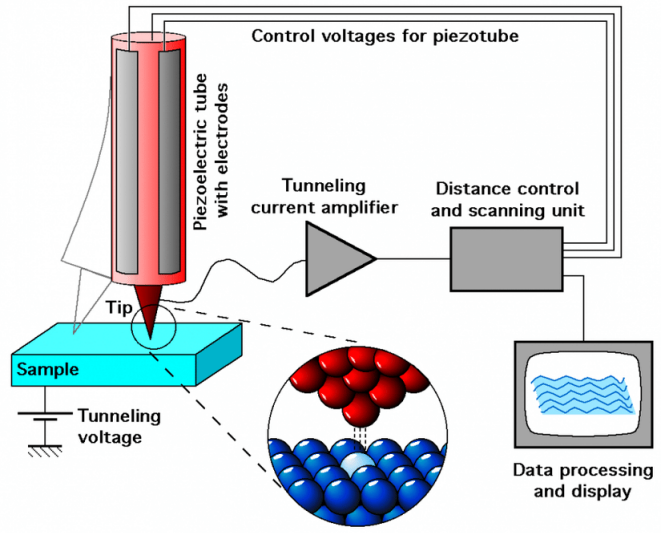

Figure 2.1: *Schematic overview of an STM-setup. [17].*

2.1.1 STM-Tip

A first part of the setup to delve into more deeply is the STM-tip, as there are a few requirements that such a tip should adhere to. These involve both the shape of the tip as the material that is chosen.

The material that a tip is made out of should abide by two conditions [18]. Firstly, the material should be a free-electron metal. Secondly, the material should have a DOS that is as flat as possible, as is shown by the Tersoff-Hamann model [19, 20].

Ideally, one wants the tip to be as sharp as possible, such that the apex of the tip is of a nanometric scale [18]. Obtaining such a sharp tip is not realistic in practice, but it is important to strive for it to be as sharp as possible. When the apex is thicker, a tunneling current will occur over a larger area, causing a lower spatial resolution.

The preparation of such a tip can be done in multiple ways [21–25]. One example is cutting, where a wire cutter is used at an angle of $\sim 45^{\circ}$ to manually cut a wire into a sharp tip [21]. Another method is DC electrochemical etching [22], which will be elaborated upon further in Sec. 3.1.1. A method can be chosen dependent on the choice of material and environment in which the tip is used.

If an STM setup is placed within a dilution fridge that can cool down to sub-kelvin temperatures, one can consider to choose a tip material that is superconducting under these conditions [25]. Once a superconducting tip is used, one creates an SNN Josephson tunnel-junction between the tip and sample (or an SNS junction, if the sample is also superconducting). By performing IV-curve analysis, a method becomes available to see whether the tip has reached its critical temperature [5].

2.1.2 Sample

When performing tests on STM-instrumentation, sample choice can become somewhat arbitrary, as long as its of good enough quality that it can actually be used for STM-experiments. In this case, it is the best option to choose a sample that is easy and forgiving to work with, which comes with a few requirements that the sample should comply with. Firstly, one can consider to work with a material that has a well-known and recognizable lattice structure. Secondly, the sample should be approximately inert, and easy to handle and prepare. Finally, if the sample contains very steep inhomogeneities, such as grooves or large incisions, it could lead to problems during scans, which should therefore also be prevented.

It could also be interesting to choose a sample that is superconducting at low temperatures, when a superconducting material is taken for the tip [25]. This way, one could turn the STM-junction into an SNS Josephson junction, which could for example be interesting to examine the non-zero conductance anomaly in Scanning Tunneling Spectroscopy at extremely low temperatures [26].

2.2 Piezoelectric Elements

Each STM will contain some kinds of piezoelectric elements: piezoelectric tube scanners to perform STM scans, sense piezos to measure for tunneling currents, and sometimes the attenuators responsible for moving the tip are of a piezoelectric nature.

The principle behind these piezos is the inverse piezoelectric effect: by applying a voltage V over a side of a rectangular piece of piezoelectric material, a strain is generated. The normal strain is defined as (analogous for y and z):

$$\varepsilon_x \equiv \frac{\delta x}{x} \tag{2.2}$$

Version of July 7, 2023– Created July 7, 2023 - 11:30

A relation between the applied voltage and generated strain can be formulated via the piezoelectric constant. It is defined as the ratio between a strain component and a component of the applied electrical field density [27]. For example:

$$d_{zx} \equiv \frac{\varepsilon_x}{E_z} \tag{2.3}$$

which relates to the voltage via $E_z \propto V$.

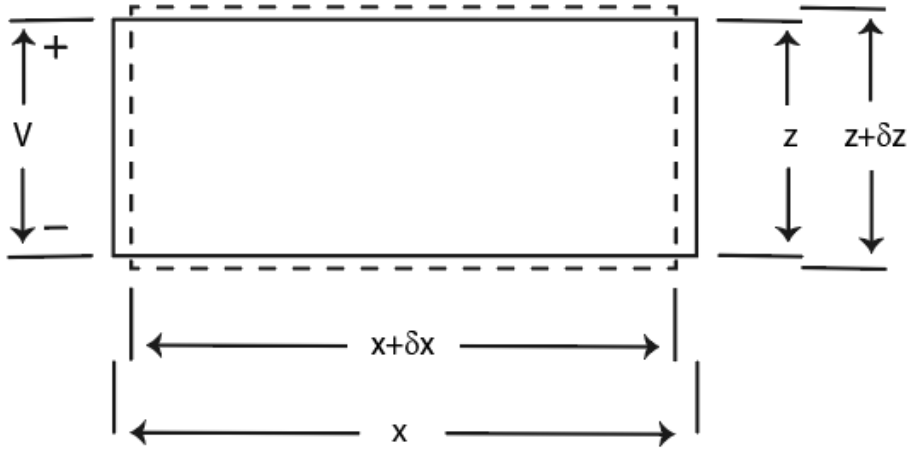

Figure 2.2: *Two-dimensional depiction of the inverse piezoelectric effect. A voltage V is applied, which in turn generates a strain in all directions on the piezoelectric material.*

Piezoelectric elements also contain capacitances. It can be taken as a general rule that the strain also scales with the capacitance, and thus $\varepsilon \propto CV$. At cryogenic temperatures, this proportionality can become an issue [28]. The capacitance of piezos can drastically decrease at such temperatures, meaning that the extension of the piezo will also severely reduce. This decrease needs to be taken into account when working with a piezo in a cryostat; tips can approach and retract at room temperature (RT), but might not move when the temperature gets too low.

Two simple examples of a piezo used in STM are the lift piezo and sense piezo. These are both used in STM to provide a small motion in one direction.

2.2.1 Slip-Stick

The slip-stick motion is a method for the approach that is commonly used in STM (e.g. [29, 30]). A piezoelectric element is clamped in between the

'fixed world' and the experiment. The latter two are commonly pulled towards each other by means of a spring, such that tightness can be adjusted. Once a voltage is set over the piezo, it will experience a strain, which in turn exerts a driving force F_d on the experiment. There is also a frictional force F_w exerted on the experiment. Once $F_d > F_w$ for a certain strain, the experiment will 'slip' away, whereas if $F_d \leq F_w$, the experiment will 'stick' in place. Since slip-stick involves much friction, it should be noted that a lot of heat dissipation comes along with it.

Consider using a trapezoidal wave as the pulse driving the piezo. Note that the slope of trapezoid sides determine the magnitude of the driving force. In this case, the driving force forward and backward is equal, by which there will be no net displacement for the experiment. This motion would be a 'stick-stick' or 'slip-slip' maneuver. To achieve motion forward, a 'slip-stick' maneuver, the pulse needs to be altered such that the upward slope delivers a driving force $F_d > F_w$, while the downward slope exerts a driving force $F_d < F_w$ (other way around for stick-slip).

In a vertical configuration, gravity also plays a role. To move the experiment upwards, the driving force should be $F_d > F_w + F_g$. On the other hand, to move the experiment downwards, the driving force should be $F_d > F_w - F_g$.

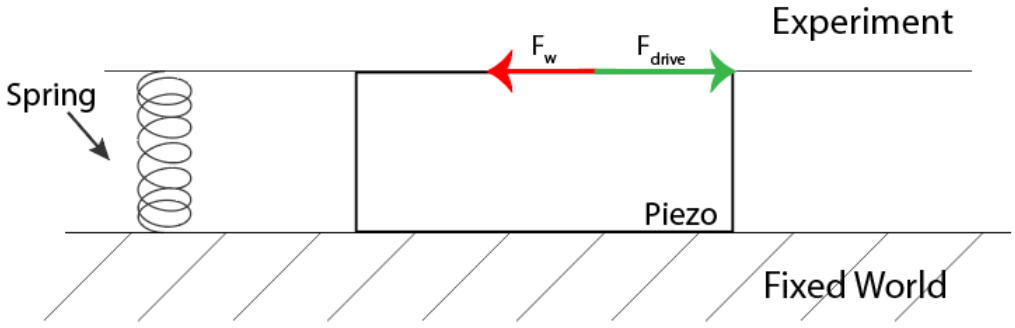

Figure 2.3: *Schematic for slip-stick. Due to the strain of a piezo, a driving force F_d is exerted on the experiment, while a frictional force F_w is exerted in the opposite direction.*

2.2.2 Tube Scanner

To perform scans, many STM's have a piezoelectric tube scanner. A tube scanner consists of an inner and outer tube, see also Fig. 2.4. The inner

Version of July 7, 2023– Created July 7, 2023 - 11:30

tube is connected to the z-voltage, which enables the tube scanner to provide a strain in the z-direction. The outer tube is divided into 4 quadrants, two for shear movement in the x-direction (via voltages V_x^+ and V_x^-), analogous for the y-direction (via voltages V_y^+ and V_y^-). These strains provide the motion required to perform scans with STM. The provided strains depend on these voltages via:

$$\varepsilon_x \propto (V_x^+ - V_x^-) \qquad \text{and} \qquad \varepsilon_y \propto (V_y^+ - V_y^-) \tag{2.4}$$

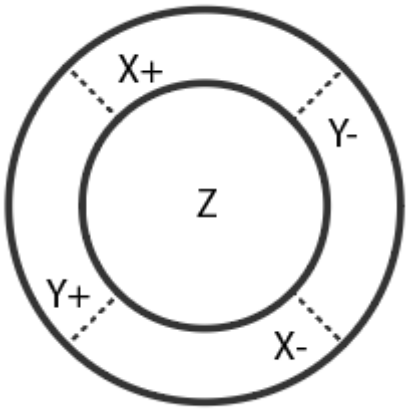

Figure 2.4: *Cross section of a tube scanner, consisting of an inner and outer tube.*

2.3 Components of the Electrical Circuit

An STM is part of a larger electronic circuit. This next section shall discuss some of the other components of such an electrical circuit.

2.3.1 I/V-Converter

Tunneling currents can be expected to be of the order $\sim$1 nA, which would require a very sensitive device to detect. Furthermore, it is more convenient to measure a voltage than a current. For these two reasons, amplification and conversion to a voltage, an I/V-converter is typically implemented into an STM setup. A gain G will be used to denote the amplification.

When a coaxial cable is used for the tunneling current towards the I/V-converter, the parasitic capacitance can be an issue due to the microphone effect [31]. The current noise caused by this parasitic capacitance is:

$$I_c = \frac{dQ_c}{dt} = C_{par}\frac{dV_c}{dt} + V_c\frac{dC_{par}}{dt} \tag{2.5}$$

where the subscript c indicates 'coaxial cable'. The parasitic capacitance of a coaxial cable is proportional with its length [32]. Considering that acoustic noise can cause deformations in the coaxial cable, a change in capacitance can occur, resulting in a current noise. It is therefore very typical for STM setups to make sure that such a coaxial cable between tip and I/V-converter is as short as possible [33].

2.3.2 Lock-In Amplifier

Once an STM-tip and sample are in very close proximity of one another, a tunneling current can be measured. Effectively, the STM-junction can be considered to be a resistor. However, apart from this resistive component to the voltage that originates from the I/V-converter, there is also a capacitive component that turns out to be useful, as it can be used to perform a so-called capacitive approach, as described by de Voogd et al. [15]. This approach uses the capacitance of the STM-junction as a measure of distance between tip and sample.

The capacitive approach requires a readout of only the capacitive component of the voltage, which is the reason why a lock-in amplifier is an excellent addition to an STM-setup. A useful feature of a capacitor is that it introduces a phase shift, whereas a resistor introduces no such phase shift. Some lock-in amplifiers have an auto-lock function that is able to use this accumulated phase difference to give a separate readout of the capacitive and resistive component of the signal, which is exactly what is desired.

Given the out-of-phase component Y, I/V-converter gain G, and lock-in reference frequency f and AC voltage V_{ref}, de Voogd poses the following formula to find the capacitance of the STM-junction:

$$C = \frac{Y}{2\pi f G V_{ref}} \tag{2.6}$$

by which also:

$$\sigma_C = C \cdot \sqrt{(\frac{\sigma_Y}{Y})^2 + (\frac{\sigma_f}{f})^2 + (\frac{\sigma_{V_{ref}}}{V_{ref}})^2} \tag{2.7}$$

Version of July 7, 2023– Created July 7, 2023 - 11:30

At distances d far from the sample (as seen from the perspective of the tip), the parasitic capacitance between the tip holder and sample dominates, as they act as a parallel plate capacitor

$$C \approx \frac{\epsilon_0 A_{par}}{L_{par} + d} \tag{2.8}$$

with ϵ_0 the permittivity of free space, A_{par} the surface area of the tip holder, and L_{par} the length of the tip outside of its holder (thus $L_{par} + d$ is the distance between the tip holder and sample). When the tip gets closer to the sample, the shape of the tip apex will start to play a role and eventually dominate; as the apex is not infinitely thin, it will function as its own parallel plate capacitor that will be dominant at a close enough distance from the sample. To get a reference of what this looks like, see Fig. 2.5.

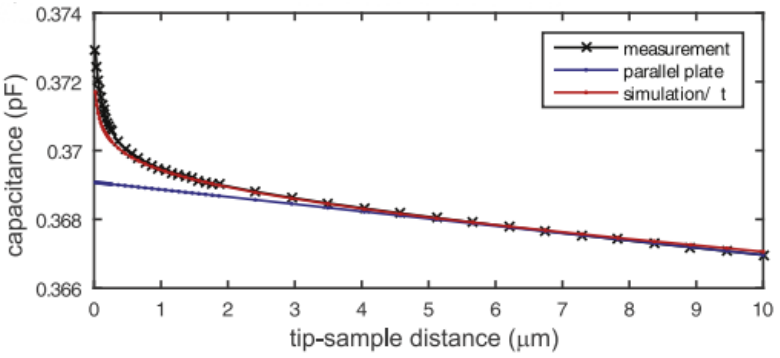

Figure 2.5: *Tip-sample capacitance as simulated and measured by de Voogd et al. for a Joule Thompson STM (JT-STM) [15]. The blue line represents a lower boundary parallel plate capacitance between sample and tip-holder. The performed measurements (black) seemed to agree well with the simulations (red).*

2.4 Cryostat

There is two different types of dilution refrigerators: 'wet' and 'dry' ones. The difference between a wet and dry dilution refrigerators the method used for precooling. A wet dilution fridge precools by use of cryogenic fluids; liquid nitrogen at 77 K and a liquid ^{4}He-bath. This method requires a constant input of ^{4}He, which is time-limiting as the available amount of cryogenic fluid is finite. A dry dilution fridge on the other hand, makes use of a cryocooler as the method of precooling. Such a device uses alternative methods to cool down instead of cryogenic fluids. Dry dilution refrigerators bring along the advantage that they are closed systems, which means

that they could theoretically continue to run forever. An example of a cryocooler is a pulse tube (PT) [34]. A PT operates by pumping ^{4}He through the system in a cycle of compression and decompression. The downside of a PT is the mechanical vibrations that it brings.

A dilution refrigerator has multiple plates, of which the bottom four are shown in Fig. 2.6. The 4K-plate is only subjected to the precooling, by which it can reach temperatures around 4 K. To further cool down the lower plates, a mixture of ^{3}He and ^{4}He is used, which is pumped into the mixing chamber (MC) that resides on top of the mixing chamber plate (MC-plate). Within the MC there is an equilibrium between He in a concentrated and dilute phase. Once ^{3}He crosses the phase boundary separating these two phases, the ^{3}He dilutes, which costs energy. This energy is taken from the environment, resulting in the cooling power for the MC-plate.

As ^{3}He-atoms are fermions, and ^{4}He-atoms bosons, more atoms of the latter can occupy the ground and first excited states. This fact results in the boiling point of ^{3}He being lower than that of ^{4}He. Considering that the mixture is gaining energy because of the dilution, its entropy rises. Temperature and pressure are regulated in a way, such that this entropy increase results in the vaporization of mostly ^{3}He. This vaporization happens in the still, which is located on the still plate. A pump circulates the vaporized He back towards the MC. To regain an equilibrium, ^{3}He in the concentrated phase is diluted again, by which the cycle repeats itself.

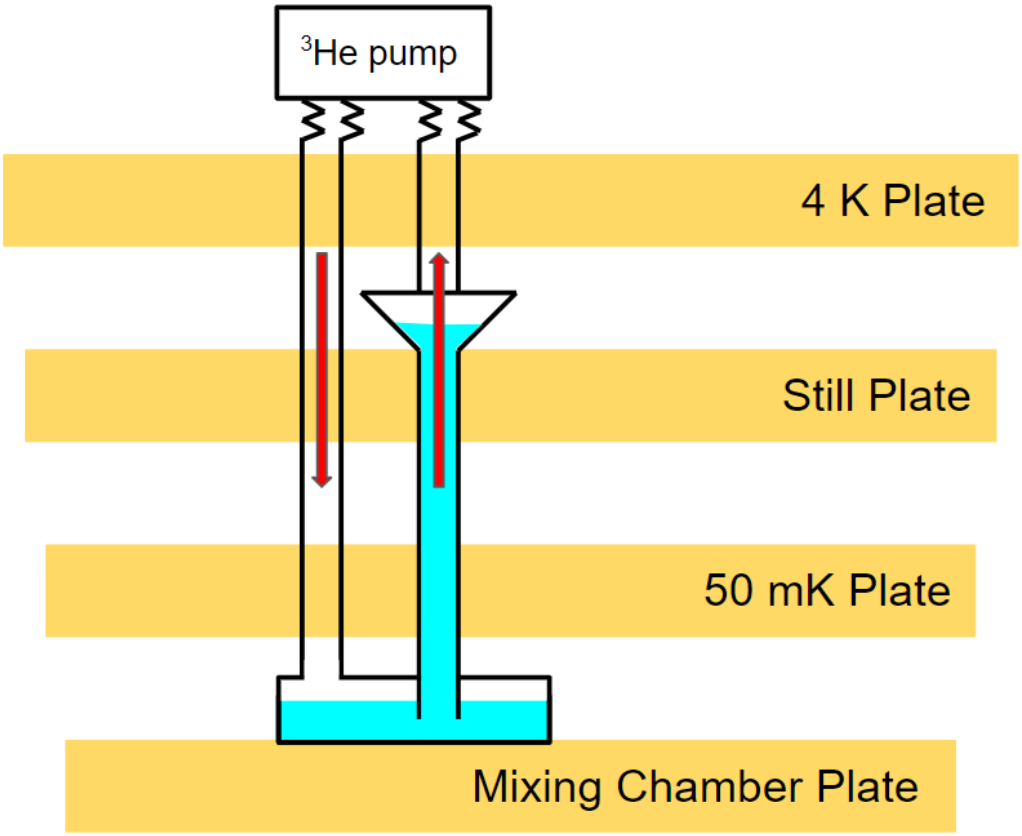

Figure 2.6: *Schematic of a dilution fridge's lowest four plates, including the system that takes care of the ^{3}He circulation. The 4K-plate is precooled with ^{4}He (wet) or a cryocooler such as a pulse tube (dry), whereas the rest of the plates obtain their final temperature due to the processes happening in the mixing chamber and still. Liquid He is shown in blue and the flow of He gas is indicated with red arrows [35].*

Chapter 3

Methods

Within this chapter, a discussion is presented on how to use an STM-setup to obtain a scan. The first step is to prepare an STM-tip to use as a probe in the two used STM's: the probehead STM (PH-STM) and the Basic STM. The process of obtaining an STM-scan can be divided into 4 steps: a coarse approach to make some large steps at the start, a fine approach to diligently reach a tunneling current, a feedback system to stay at a constant tunneling current and finally the scan itself.

The methodology for the PH-STM and Basic STM is mostly the same, apart from the motors that are used in the STM's to make the tip stage move, and a segment of the manner of controlling these drivers. The entire process from the fine approach will be regulated with a program called *CAMERA* (Computer Aided Measurement Environment for Real-time Atomic imaging), which has been designed by the Electronics Department (ELD) at Leiden University, in cooperation with Leiden Probe Microscopy (LPM) [36]. *CAMERA* is able to control the STM's via a set of drivers that are contained in a rack that will fittingly be referred to as the 'LPM-rack'.

3.1 Tip & Sample Preparation

Before any STM can be performed, it is necessary to choose and prepare a suitable STM-tip and sample. This section shall discuss the required methodology.

3.1.1 STM-Tip

The tip material that was chosen for this project is tungsten (W). Tungsten is a free-electron metal and has a flat DOS at the Fermi-level, causing it to be suitable as material for an STM-tip. It is also known to be very hard, which makes it easier to work with [37]. W, together with Pt-Ir [23], is one of the most commonly used materials for STM-tips [38]. To obtain a qualitatively good tip, tungsten can be DC electrochemically etched with NaOH or KOH as the used base [24]. Tungsten oxidizes rather quickly [39], meaning that they should regularly be replaced if one wants to obtain high resolution scans. Note that it won't oxidize in vacuum, which it is in inside the cryostat during and after cooldown.

For the DC-electrochemical NaOH-solution was chosen to work with, as it is less aggressive than KOH and thus safer to work with. The etching station that was used, was borrowed from the van Ruitenbeek lab at Leiden University. The wires that are used for the tips in the PH-STM and the Basic STM are of 5mm⌀ and 1.25mm⌀ respectively. These thicknesses were chosen for being the best fit in their respective tip holders.

A schematic of the setup can be seen in Fig. 3.1. To prepare the wire, it needed to be cleaned first to remove greases and other organic materials. The existing oxide layer was scraped off with sanding paper, after which it was placed in a sonicator, in a glass container filled half with acetone, half with isopropanol. After it had been in the sonicator for $\sim$10 minutes, it was rinsed with acetone, followed by isopropanol and purified water. The gold loop that is used in the setup got the same treatment with the sonicator.

The wire is placed in a clamp and is guided through a wire guide, to ensure that the tip will hang perpendicular to the gold ring. To obtain $\sim$1 cm tips, the wire sticks out under the gold loop by this amount. The gold wire and tungsten wire are connected to the DC-power supply by use of two alligator clips, with the gold wire acting as the cathode, and the tungsten wire consequently as the anode. A measuring cup filled with shaving cream is placed below the wire and gold loop to catch the tip once it falls, without damaging it.

Version of July 7, 2023– Created July 7, 2023 - 11:30

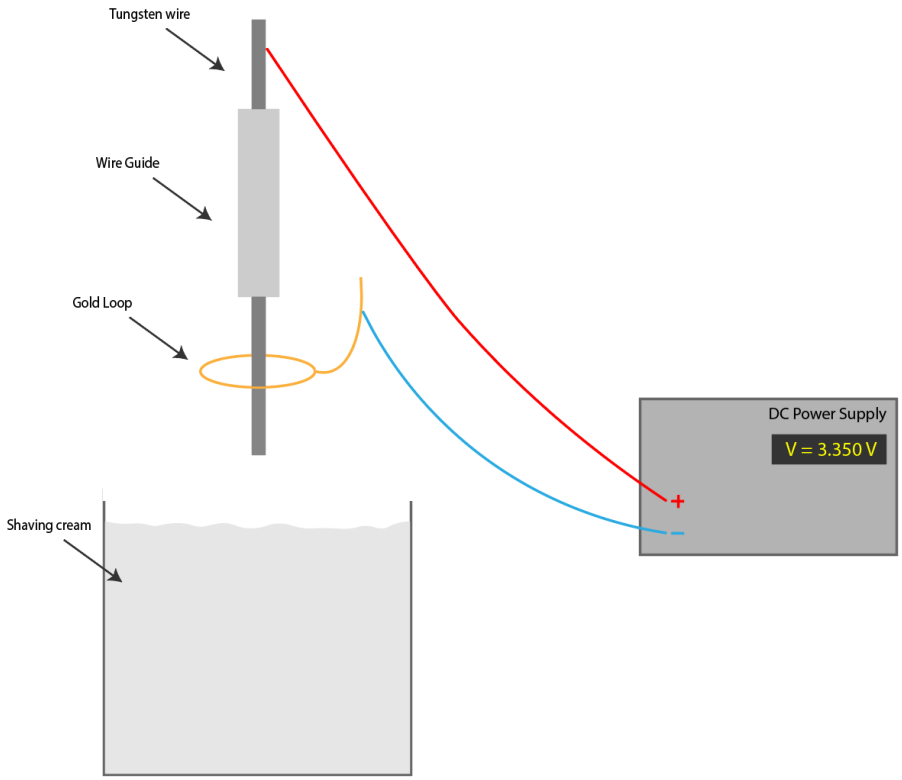

Figure 3.1: *Schematic of the setup for DC electrochemically etching. The gold wire and wire guide are in reality held by two clamps, attached to a base behind the setup, to keep them in place. These clamps were kept out of the image to keep the image clear.*

A 1 M NaOH-solution was prepared under a fume hood. To start the etching process, a thin film of the NaOH-solution is applied to the gold ring, and the DC-power supply is turned on at 3.350 V. During the etching process, the following electrochemical reactions take place [24]:

$$\text{(Cathode:)} \quad 6H_2O + 6e^- \rightarrow 3H_2(g) + 6OH^- \tag{3.1}$$

$$\text{(Anode:)} \quad W(s) + 8OH^- \rightarrow WO_4^{2-} + 4H_2O + 6e^- \tag{3.2}$$

$$\text{(Overall:)} \quad W(s) + 2OH^- + 2H_2O \rightarrow WO_4^{2-} + 3H_2(g) \tag{3.3}$$

The tungsten that is etched off of the tip turns into the salt WO_4^{2-}, that precipitates onto the gold loop. The gold loop is therefore carefully cleaned on occasion with a Kimtech™ wipe (after turning the DC power supply off). It should also be noted that H_2-gas is released as a byproduct.

The amount that is released is not at all dangerous, but the experiment could be done in a fume hood if one prefers to do so.

The observed tip shape arises from the meniscus that the NaOH-solution will create due to surface tension. As the concentration of OH^- is higher at the base of the meniscus than at the top, the rate of etching is enhanced, causing the tip to take shape. Eventually, the tensile strength in the wire cannot sustain the weight of the tip underneath the gold ring, and the tip will drop [24].

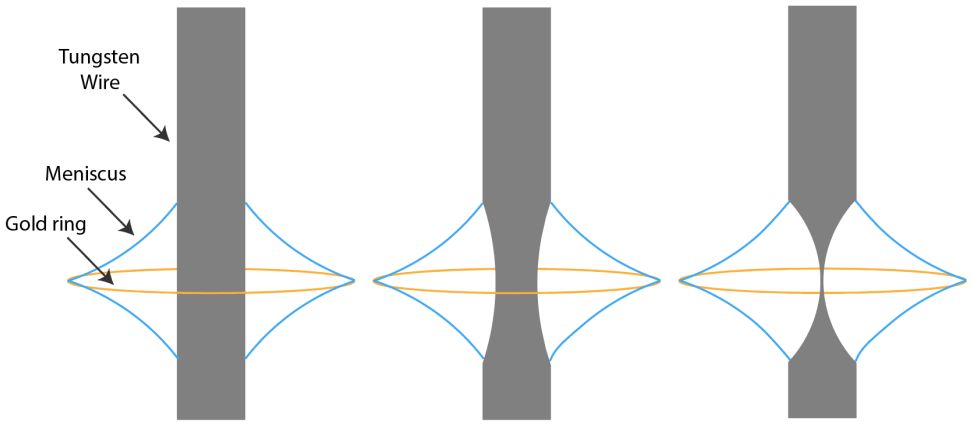

Figure 3.2: *Schematic of the etching procedure. In the first image, a meniscus has been applied, after which the tungsten wire is etched over time until the tip breaks off.*

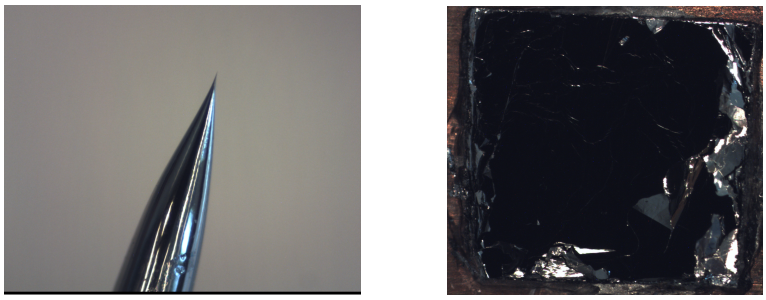

(a) ***(b)***

Figure 3.3: *One of the STM-tips (a) and one of the HOPG samples (b). The images were made via an optical microscope.*

3.1.2 Sample

A material that complies with all of the requirements mentioned in Sec. 2.1 is graphite. The lattice structure of graphene (a monolayer of graphite) is well known to be of an hexagonal nature and has two lattice constants $|\vec{a_1}| = |\vec{a_2}| = 2.46$ Å [40]. The used material within this project is HOPG, Highly Oriented Pyrolytic Graphite. The advantage of this type of graphite is the low mosaic spread angle (0.3°-3°) [41], causing the terraces of the lattice structure to be considerably flat. This material is also relatively inert, making it easy and forgiving to work with [42]. HOPG can be cleaved with scotch tape, which makes it easy to prepare for STM-experiments. Note that HOPG is not a superconductor.

To prepare HOPG, the sample can be 'cleaved'. Graphite is a Van der Waals material, meaning that the only force keeping layers of graphene together is the Van der Waals force. This property allows for the use of scotch tape to cleave off a few layers of graphene at a time, making sample preparation very practical: once a sample is damaged, cleaving it a few times should in turn make it smoother until it is usable again. One of the HOPG samples, after it has been cleaved, can be seen in 3.3b.

3.2 Coarse Approach

The first step towards obtaining an STM-scan is the coarse approach. The tip will have to travel a relatively long distance as compared to the eventual distance between tip and sample. If the start of the approach would be as slow as the final stages of the approach, the entire process would take too much time. Therefore a capacitive approach (See also: Sec. 2.3) can be used to take the first, coarse steps, as described by de Voogd et al. [15].

The progression of the measured capacitance during the coarse approach can be used as an indicator for when to initiate the fine approach. When the capacitance between tip apex and sample is seen to start dominating, it is best to stop the coarse approach and move on to the fine approach. This method ensures that a lot of time is saved in the first stages of the approach and makes it possible to make larger steps safely.

The lock-in amplifier that complies with the in Sec. 2.3 mentioned desires, and that was used during this project, is the *Stanford Research Instruments SR830* [43]. This lock-in is fully analog, meaning that other instruments are necessary to digitize the measurements. The device has an accuracy of $\sigma_{V_{ref}} = \pm 1$ mV and $\sigma_f = \pm 0.01$ Hz . For the capacitive readout, both STM's use a National Instruments (NI) myDAQ [44] to digitize

Version of July 7, 2023– Created July 7, 2023 - 11:30

the data. The I/V-converter used to amplify and convert the current to a voltage is a *FEMTO DLPCA-200* [45]. The maximal gain of this device is $G_{max} = 10^9$.

To obtain an absolute capacitance of the STM-junction, one measures the out-of phase component Y of the voltage originating from the I/V-converter with the lock-in. To amplify Y, an AC bias voltage V_{AC} is sent along with the DC bias. This AC bias voltage is later set to zero during the fine approach. During the measurement of Y, Eq. 2.6 can be used to convert said voltage to a capacitance. This capacitance can then be plotted as a function of the amount of taken steps to obtain a visualization of the approach while it is running.

3.3 Fine Approach

After the coarse approach has been completed, it is time to approach more delicately. For this reason, the fine approach procedure consists of 2 alternating parts: a sense and a coarse step. A schematic of the fine approach procedure can be seen in Fig. 3.4

The fine approach always starts with a sense, through a full extension of the sense piezo. This sense is done to show if the tip is (accidentally) already in the tunneling regime. To be able to make this claim, the measured voltage is compared to a voltage limit that is defined beforehand. If the tip senses a voltage that is above this threshold, the fine approach stops. If on the other hand the setpoint isn't reached, the sense piezo gets fully retracted. After this retraction, a coarse step is made. The size of this step should not exceed 0.4 times the size of the full sense piezo range, to ensure that the coarse step doesn't push the tip fully through the range in which a tunneling current can be measured. When this step is completed, a new sense is performed and the process repeats itself again and again until eventually a tunneling current is measured.

As mentioned earlier, the fine approach is regulated through *CAMERA*. Once *CAMERA*'s 'approach mode' is turned on, the fine approach becomes fully automated and it automatically stops once a tunneling current is measured. Once a successful sense has occurred, two more manual senses are performed to confirm that there is in fact a tunneling current. After approach mode is turned off, the sense piezo will be extended towards the location where a tunneling current was last sensed and is placed in feedback to ensure a constant current.

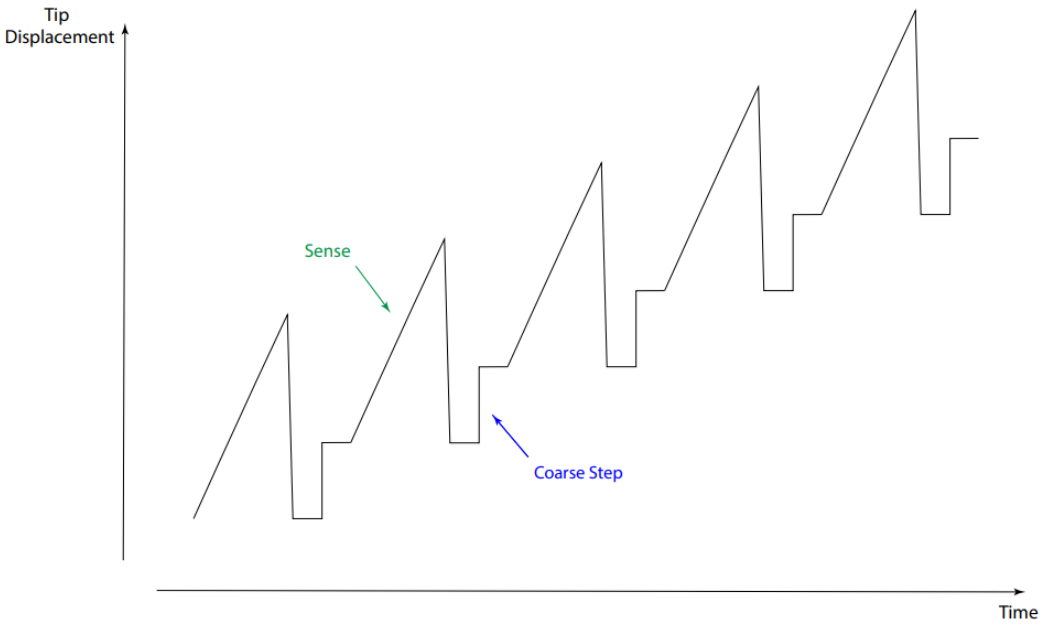

Figure 3.4: *Schematic of the procedure of the fine approach. Each sense is followed by a coarse step.*

3.4 Feedback & Constant Current

To be able to perform a scan later on, it is essential to ensure that the tip can be kept at a constant distance from the sample (and thus at a constant current). To facilitate this constant distance, PI-feedback is used to keep the tip at a pre-determined voltage setpoint. The PI-controller that regulates this feedback system is one of the parts of the LPM-rack.

The proportional part of PI-feedback is used to rather roughly work towards the predetermined voltage setpoint. The integral feedback provides an integration, effectively averaging the signal out to lower deviations from the setpoint. A derivative attribution could also be added to perform PID-feedback. This term would be able to compensate for very large changes in voltage, due to for example large inhomogeneities in the sample. The derivative term is however deemed to not be necessary, as the sample can be cleaved to prevent such large grooves.

To allow for (proportional) feedback on a current that is exponentially dependent on distance, a logarithmic amplifier is used, that is part of the LPM-rack. It located after the PI-controller, as the controller still does a comparison to a voltage setpoint for proportional feedback.

3.5 STM-Scan

Once the tip is in feedback in the tunneling regime, it is possible to perform a scan. By using the tube scanner, the tip is moved above an area with predetermined dimensions at a constant distance from the sample. The voltage that is applied w.r.t. the voltage setpoint to the lift piezo to compensate for the structure of the sample, is a direct measure of relative height differences in the sample. By mapping these voltages as a function of position, one effectively creates a 2D-plot of the surface topography.

To see if a scan is an actual scan of the surface, and not noise that is being measured, two scans are made at once: left-to-right (L2R) and right-to-left (R2L). When a scan is started, it starts by doing one line of L2R, after which it repeats the same line backwards, R2L. If these two scans show good resemblance, it may be assumed that an actual scan of the surface is being performed, due to the fact that noise is of a random nature.

To be able to obtain atomic resolution in a scan, the distance between pixels should be smaller than the lattice constant of the material. For example, for HOPG, with a lattice constant $a = 2.46$ Å [40], the distance between pixels should ideally be less than half of that, say <1 Å, to obtain a qualitatively good image.

3.6 PH-STM & Basic STM

As mentioned, two types of STM are being used during this project, the PH-STM and the Basic STM. One major part distinguishes the two: the motors that are responsible for making the tip stage move. Nevertheless, the rest of the setup is close to identical.

3.6.1 Probehead STM

The PH-STM, that was designed by LPM, owes its name to its distinctly shaped encasing, the probe head (see also: Fig. 3.5). With the wider half of the probe head as the top side, the tip stage is located within the bottom part of the device, with the tip pointing up towards the sample. The tip stage and sample can be lowered through an opening at the top into the probe head and locked in place by use of bayonet mounts. The opening can in turn be closed with another bayonet mount. This specific design allows for the attachment of an elevator system that enables the already performed in-situ [46], but also the new 'in-operando' tip exchange and sample preparation. This would make it possible to perform these two

actions, while the dilution refrigerator remains turned on. The special design of the elevator allows for use in a dry dilution refrigerator, without compromising any part of the vibration isolation system (VIS) of the cryostat.

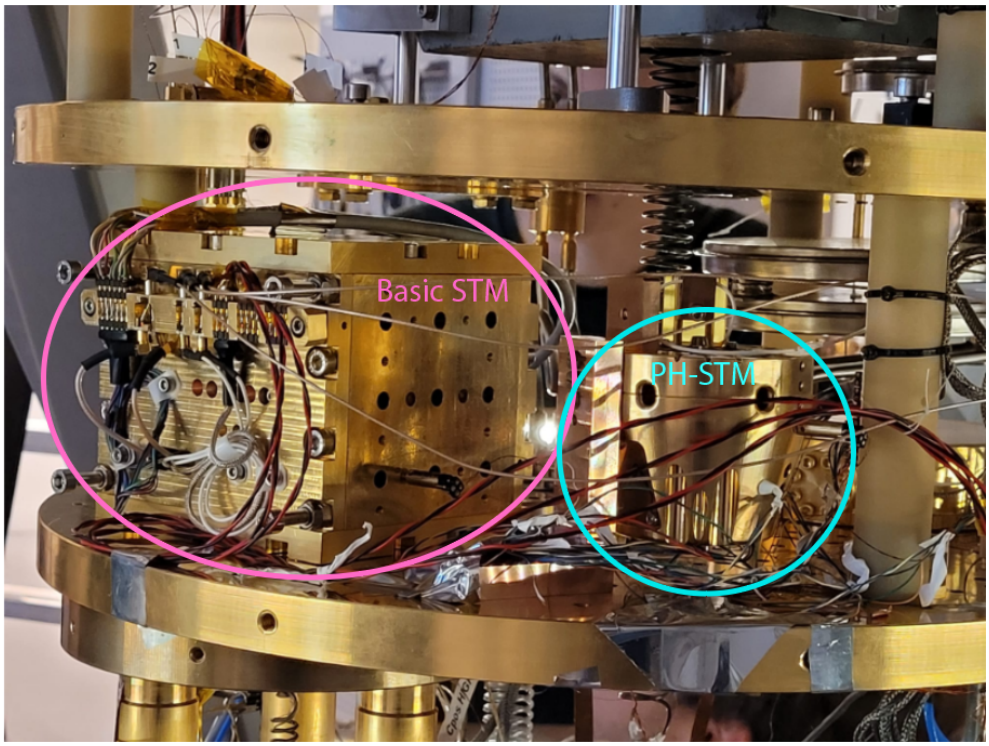

Figure 3.5: *Image of the Basic STM and PH-STM, placed atop the MC-plate.*

The PH-STM makes use of six slip-stick piezo actuators. These actuators are distributed evenly along the sides of the stage that the tip stage is inserted into, in pairs of two: the 'PAN-configuration'. To perform a coarse step, all six actuators start their slip-stick motion at once, pushing the stage upwards. For stability reasons, not all the actuators end the maneuver at the same time; they all retract one by one to keep the stage more stable when compared to all six retracting at once.

A disadvantage of using the PAN-motor is the occurrence of (lots of) friction due to the slip-stick maneuver being used. This could in turn result in lots of heat dissipation, which could prevent a large amount of steps in short time intervals at low temperatures, due to too much heat build-up for the dilution refrigerator to handle.

It is expected that the capacitances of the piezoelectric elements of the PAN-motor will drop to ∼20%-33% of the original capacitance as has been

determined earlier by K. van Deelen of the Oosterkamp Group at Leiden University. Other piezoelectric elements beside the PAN-motor that are contained in the PH-STM, are a sense piezo to sense for tunneling currents, and a tube scanner to perform scans.

To drive the actuators, a specially designed motor driver is used. This driver was designed to send signals specifically for the PAN-motor. These signals are regular slip-stick pulses, apart from the fact that it has six slopes downwards, separated by an equal amount of time; one for each of the piezos. The max voltage output of the motor driver is 240 V, but as the scope that is used to do a read out of the driving signal gives the voltage in V_{pp}, the signal voltage will be referred to in this unit. Hence, the maximal voltage output of the driver is $V_{max} = 480\ V_{pp}$.

3.6.2 Basic STM

The other STM that is used in this project is the Basic STM, which has also been designed by LPM. The STM is encased within a massive copper box, that has been coated with gold paint. The movement of the tip is parallel to the ground, meaning that the tip and sample are placed at a 90° degree angle with respect to the PH-STM. This positioning accommodates for the newly designed 'linear cryo-walkers', from Onnes Technologies.

The goal with the Basic STM was to test the performance of these new linear cryo-walkers at sub-kelvin temperatures. The walker consists of two pairs of lift piezos, both attached to a separate shear piezo. To move, two diagonally displaced piezos lift up, and the shear piezos moves these two 'legs' forward, after which they come back down again. Afterwards, the other pair of legs does the same. This way of walking offers more stability than for example the alternating movement of the front and back pair of legs.

Since the Basic STM contains piezoelectric elements as well, capacitances shall again decrease under cryogenic conditions. No specific percentages are known (yet), but for simplicity reasons, the same decrease shall be assumed as for the PH-STM: a decrease towards ∼20% to 33% of the original capacitance. The Basic STM also has a pulse tube scanner and a sense piezo.

With the Basic STM comes a motor driver made by Onnes Technologies, accompanied by a Labview program made by LPM. The driver allows for maximal voltages $V_{lift,max} = 300$ V and $V_{shear,max} = 320$ V on the lift and shear piezos respectively. The voltages to be applied can be adjusted with the Labview program. It further allows for switching between

approach & retract mode, and allows for tinkering with the pulses sent to the piezos.

The cryo-walkers have a major advantage compared to slip-stick actuators: during their walk they cause close to no friction. This method of moving forward in turn results in the fact that close to no heat dissipation occurs, which should allow for approaches at sub-kelvin temperatures, whereas normally the approach in a dilution refrigerator is performed above 4 K, due of the friction of slip-stick motors.

Chapter 4

Room Temperature PH-STM

The PH-STM had to be tested at RT first, before it could be mounted into the cryostat, unlike the Basic STM, whose performance at RT was tested externally. These tests for the PH-STM include tests for the general methodology, tests for the optimal orientation of the experiment and tests to get an idea of the expected performance at low temperatures.

4.1 Capacitive Approach

The first test that was done, is to see whether the capacitive approach works as expected. A capacitive approach will be performed, until a crash is registered through an overload in Y, to make sure that the tip can move all the way to the sample. The approach was performed with $V = 480$ V_{pp}, a Gain $G = 10^9$, a DC bias $V_{DC} = 100$ mV and an AC bias $V_{AC} = 100$ mV, at a reference frequency $f = 877$ Hz.

The approach was successful and a crash was registered. Afterwards, a retraction and a new approach were performed. The readout of the out-of-phase component Y is shown in Fig. 4.1a & 4.1b. It shows the expected behavior as described by de Voogd et al. and as discussed in Sec. 2.3. These values for Y are also converted to an absolute capacitance via 2.6, and are shown in 4.1c & 4.1d.

4.2 Fine Approach & RT Scans

With the capacitive approach working well, it is time to move towards a tunneling current and a scan. A fine approach is done at $V = 240$ V_{pp}, 1

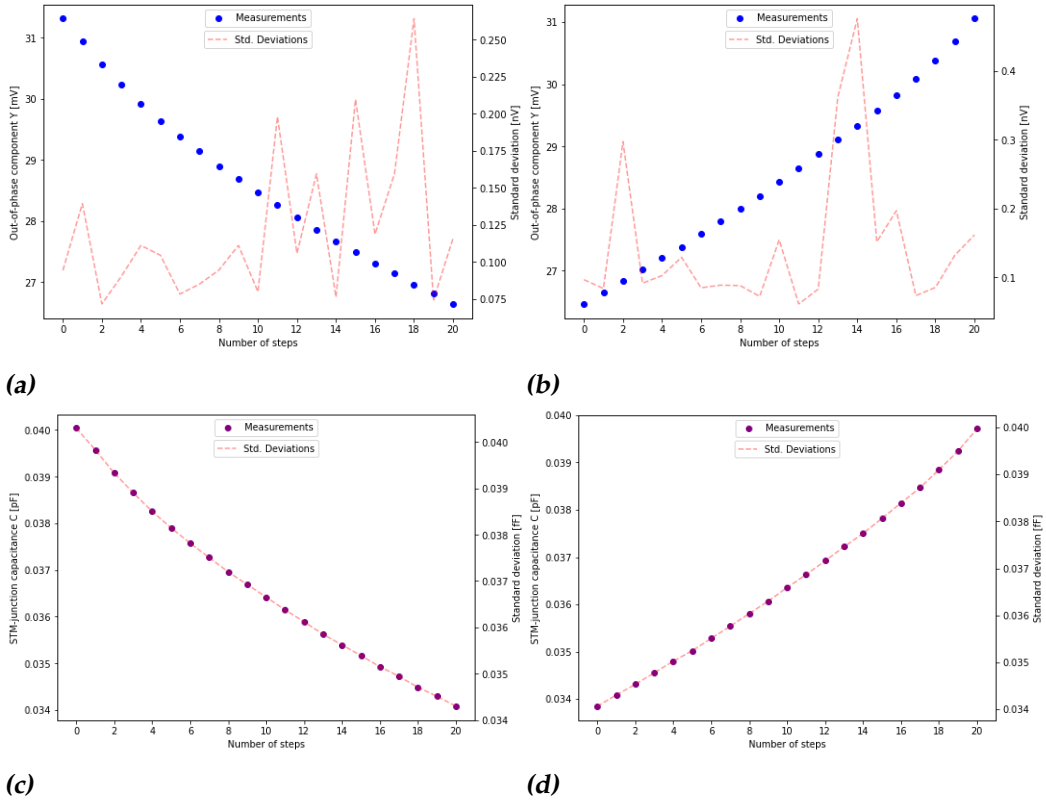

Figure 4.1: *Display of the retraction and approach with the PH-STM at 480 V_{pp}. (a-b) show plots of the out-of-phase component Y, whereas (c-d) show the absolute capacitance C.*

step at a time, each followed by a sense. The fine approach is done with a gain $G = 10^9$, DC bias $V_{DC} = 100$ mV and zero AC bias. A current threshold of $I = 1.0$ nA seemed justified, as the sense measurements at a non-tunneling distance from the sample would not exceed $I = (0.55 \pm 0.10)$ nA.

Eventually, a tunneling current was indeed measured and confirmed by two more manual senses. Approach mode is turned off, after which feedback automatically starts. For this run, a voltage setpoint $V_{set} = 3.51$ V was used, with PI-feedback parameters $P = -29.1$ dB and $I = 7.33$ Hz, and an LPF cut-off frequency $L_{LPF} = 991$ Hz. As the PI-parameters and V_{set} can only be adjusted physically on the LPM-rack, the determination of their values was a matter of slowly working towards the subjectively best signal on the scope, which resulted in the aforementioned values. Subsequently, a scan was performed for a sample area of 250x250nm, with an image at 256x257px resolution (See Fig. 4.2).

With HOPG being a 2D-material that is cleaved with scotch tape, one would indeed expect to see terraces when scanning at such a distance from the sample. The cleaving will after all not result in a perfectly homogeneous sample. As these terraces are observed, it is a good indication that this scan was successful.

A next and final step at room temperature can be to obtain atomic resolution images. Some adjustments are required however to get to this milestone. For starters, the STM can be placed in a more vibrationally isolated environment. An available object that can accommodate such vibration isolation is the Acoustic Vibration Isolation Box, or AVIB for short. The AVIB is a box that is hanging by four bungee cords, that is able to compensate for acoustic vibrations. The bungee cords effectively act as a low-pass filter, while the STM moving along in a local inertial frame in the box should lower the effect of low-frequency vibrations.

Due to deadlines concerning the upcoming cold run of the cryostat however, no time was left to find a significant enough improvement for the scans.

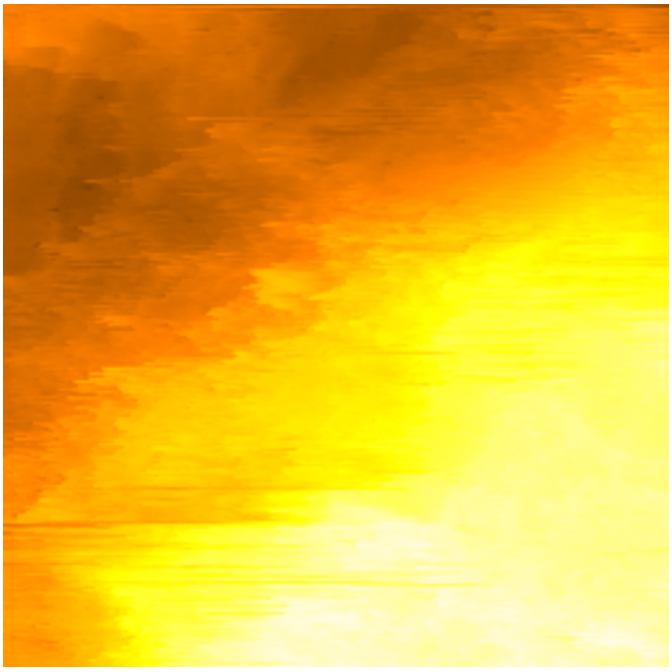

Figure 4.2: *The first successful scan at 250x250nm, 256x256px; V_{set} = 3.51 V, I = 7.33 Hz, P = -29.1 dB & f_{LPF} = 991 Hz.*

4.3 Testing for Expected Cryostat Performance

Before the PH-STM can go into the cryostat for a cold run, it is necessary to gain an idea of whether the tip stage will move at all when the STM is at low temperatures. Since the strain generated in the piezoelectric actuators scales with $C \cdot V$, the motor's performance can be simulated at RT. As mentioned, the capacitance is expected to decrease to ∼20%-33% of the original capacitance at cryogenic temperatures. Therefore, to simulate the movement with $C_{<1K} \sim \frac{1}{5}C_{RT}$ at V_{max} = 480 V_{pp}, one can try to perform approaches and retractions with C_{RT} at $V \sim \frac{1}{5}V_{max}$. If the tip moves at these lower voltages at room temperature, it could indicate that it will also move at max voltage under cryogenic conditions.

These measurements were performed until a voltage was reached at which the force upwards could not overcome friction and gravity. The relevant parameters are the gain $G = 10^9$, DC bias $V_{DC} = 40$ mV and zero AC bias. The relevant results are shown in Fig. 4.3.

In general, the retraction seems to go well at all voltages that were tested at. It can be concluded that the retraction should most likely show no problems in the cryostat.

The approach is a different story. It seems to be much slower than the retraction, as no upward movement could be observed under 110 V_{pp}. This difference was to be expected to some extent due to gravity also playing a role. The rate at which the approach happens should not matter, as the approach in the cryostat needs to be performed only once.

To conclude: at room temperature, tip movement in both directions can be observed up to a voltage of 110 V_{pp}, which is ∼23% of the maximal driving voltage. A 77% capacitance decrease can seemingly be compensated for, which might not be sufficient if the made assumption about the capacitance decrease was correct. The results are however good enough for the PH-STM to be considered as a part of the next cold run in the cryostat.

4.4 STM Orientation

Since the approach, the movement in the direction against gravity, seems to be the most difficult, it could be a suggestion to place the STM sideways or upside-down. If either positioning provides better observed movement, it would currently be preferred over vertical positioning.

It should be noted that a different orientation of the STM is not viable for the future, as the proposed elevator system for in situ sample prepa-

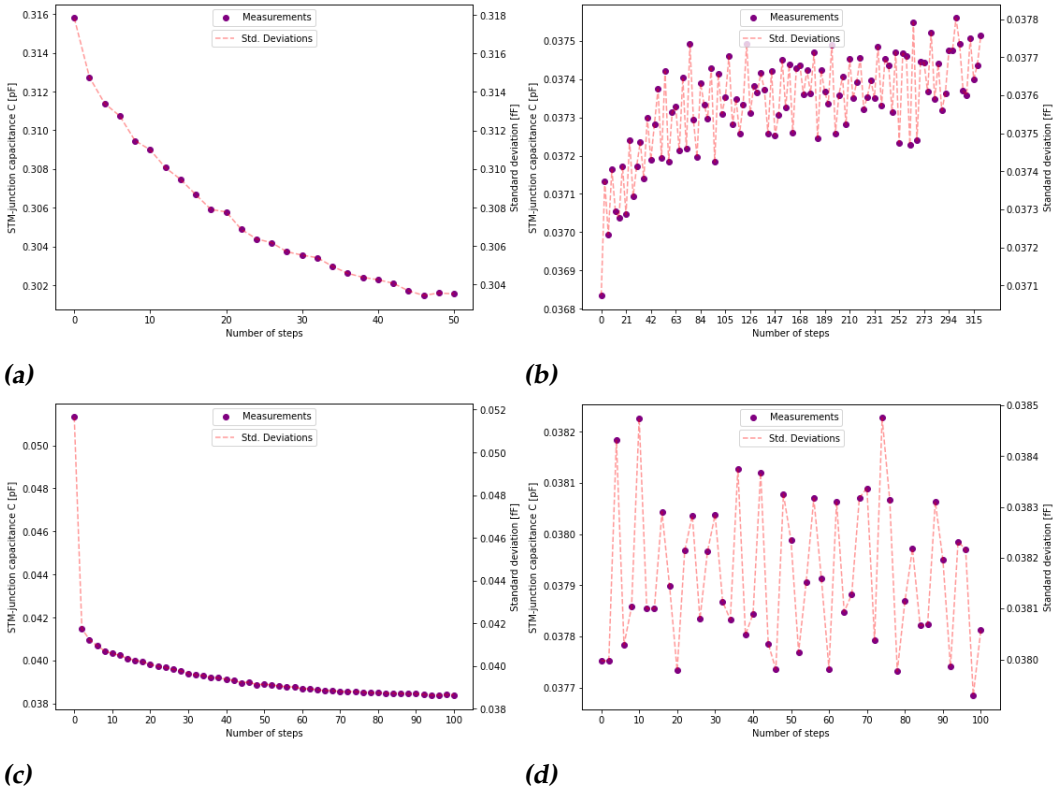

Figure 4.3: *Display of the capacitive retraction and approach at 4 chosen driving voltages. From top to bottom: (a-b) 110 V_{pp} and (c-d) 106 V_{pp}.*

ration requires for the STM to be standing right-side-up. However, the milestones that are hoped to be reached during the first cold run is only to observe movement, and to obtain a scan (at hopefully atomic resolution). The elevator system will not yet be used, and it would therefore be fine if the STM were placed horizontally or upside-down for now.

One could wonder why this more 'hacky' way is preferred over taking the STM apart and finding the problem that is causing the comparatively worse approach. This option was considered, but out of fear that taking the STM apart could give rise to different issues, and keeping the mentioned milestones in mind, the decision was made to delay taking the PH-STM apart to after the cold run.

Capacitive approaches were performed at the different orientations, but no significant improvement was observed. This result led to the decision to continue on with the regular STM orientation.

Chapter 5

Extremely Low Temperature PH-STM

With the PH-STM being tested at room temperature, and showing reasonably promising movement, it is ready to be placed in the cryostat. This chapter will discuss the performed preparations before cooldown, and the results after.

5.1 Preparation at RT

As a first step in the preparation, the entire setup was moved atop the MK-profile frame, that supports the cabinets above the cryostat. This move had to be done to avoid the presence of ground loops within the electrical circuit, whereas the cryostat itself has a common ground that can be accessed from this location. The only two components of the setup that are not located there are the *FEMTO* I/V-converter and the measurement PC that controls *CAMERA*. The *FEMTO* is placed on the inner frame of the cryostat, as this spot is the safest location in the direct vicinity of the outgoing cable trees, such that the amount of pre-amplified noise from the microphone effect can be minimized. From here, it can still be connected to the common ground. The PC is still on the measurement hall floor and is connected to the rest of the setup via optical fibers to avoid the occurrence of ground loops.

In principle, the rest of the setup with the STM in the cryostat is not that much different as compared to the RT-setup, apart from some additional wiring between the measurement devices at RT and the STM in the cryostat. An image of the PH-STM in the cryostat can be seen in Fig. 3.5.

The STM is located directly on top of the MC-plate. The probehead itself is coated with a gold layer to ensure good thermal contact with its mount, that is made of copper. The copper was polished very diligently with ethanol, while wearing gloves, as copper is known to get tarnished really easily. It would have been even better to have the contact points of the mount coated in gold as well, but due to a limited amount of gold coating, it was not possible in time before the cryostat closed. The use of gold-on-gold, gold-on-copper and copper-on-copper is very commonly used in the Oosterkamp Group to ensure proper thermal contact. This thermal contact is necessary, such that heat can flow away from the STM and can thus cool down.

To test whether the whole setup was connected correctly and is functioning well, short approach and retract tests were done at 300 V_{pp}. This test was not done for multiple voltages, as the goal was to test whether it would move at all after being installed into the cryostat at RT.

5.2 Results after Cooldown

After the cooldown for this run of the *Marshmallow* had concluded, it reached a final temperature of approximately 1 K at the MC-, 50mK- and 1K-plate, which is higher than it normally is, but low enough to perform the desired measurements. The major part of the decrease in capacitance should have happened already at higher temperatures [28].

As before, the first test for movement is the capacitive approach. A precautionary sense indicated no tunneling current in range. The motor driver was set for retraction at its maximal voltage, 480 V_{pp}. Continuous pulses were sent for 10 seconds, after which no movement was detected via the capacitive readout. This measurements was repeated once more to no avail. A next attempt was to repeat this measurement at 480 V_{pp}, but this time for 1 minute.

After the last mentioned measurement was completed, again no movement was detected. Moreover, the dilution refrigerator had been turned off automatically. During this minute of attempted retraction, the MC-plate had warmed up to 2.5K, at which point a safety mechanism in the dilution fridge is activated. At low pressure, the boiling point of a liquid drops. This decrease is also the case for liquid ^{4}He, whose boiling point will drop below 2 K under the vacuum conditions that the STM is in. Aside from the ^{3}He, also ^{4}He starts to vaporize, which will in turn be too much for the dilution refrigerator's compressor to handle; the dilution fridge gets turned off completely. The temperature rise went unnoticed, as the

temperature went up so fast, that it happened in between the automated temperature measurements on the MC-plate.

With temperature increasing within a minute, accompanied by no observed movement, it seems as if an approach at temperatures below 4 K is not feasible. This process would most likely take too long, even if the tip started to show movement after some time; even if any motion could be detected after minutes of pulses, it would have to be continuously interrupted to prevent too much of a temperature rise. The consequence is that the coarse approach with the PAN-motor should be done before the dilution refrigerator is turned on, with an attempt to keep the tip in feedback during the further cooldown. This approach would be above 4 K, meaning that there will be no vaporization of ^{4}He to cause problems.

After the cryostat had heated up back to RT, some quick retractions and approaches were attempted. Even at the maximal driving voltage, no movement could be observed, in both possible directions. This finding suggests that something malfunctioned/broke during cooldown. The reason for the malfunction of the PH-STM is yet to be found.

Chapter 6

Basic STM

The Basic STM is the second Scanning Tunneling Microscope in the project. The necessary tests at room temperature were already done by D. Coffey Blanco from LPM, having reached atomic resolution images of HOPG. The results at RT for the motors, aptly named 'linear cryo-walkers', showed amazing prowess [47]. Low heat dissipation and excellent movement at cryogenic temperatures could be expected. The next step is to examine its performance in a dilution refrigerator: do the linear cryo-walkers move well at sub-kelvin temperatures and do they allow for a scan at cryogenic temperatures in a dry dilution refrigerator?

6.1 Preparation at RT

The Basic STM itself was placed on the MC-plate of the *Marshmallow*. See Fig. 3.5 for an image of the Basic STM in the dilution refrigerator. The box containing the STM is made out of copper and coated with gold, which should ensure proper thermalization. Its contact surface is cleaned with ethanol and placed on top of the MC-plate. One day before placing the STM in the cryostat, a new tungsten tip was placed into its tip holder.

The *FEMTO* is again located on the inner frame of the cryostat, ensuring the lowest amount of pre-amplified microphonic noise. The measurement-PC that controls *CAMERA* is again placed on the floor of the measurement hall, while being connected to the rest of the setup via optical fibers to avoid ground loops.

Once in the cryostat, short approach and retract tests were performed. Movement was tested for at (V_{lift}, V_{shear}) = (150 V, 320 V) – before the black dotted line – and (V_{lift}, V_{shear}) = (30 V, 64 V), a fifth of the maximally

allowed output – after the black dotted line. Due to logistics with the *Marshmallow* – several measurements had to be done in a few hours – these were the only measurements that was time for in this run.

The cryo-walkers performed as they should, being able to move at both sets of voltages (See Fig. 6.1). With the motors running well on the last set of voltages, there is reason to be optimistic about its performance at sub-kelvin temperatures. A decrease in V_{lift} and V_{shear} by a factor of 5 results in motion that is still very noticeable. By approximating that the distance to the sample for the last approach is large, the capacitance/out-of-phase component is by approximation still linear. A linear fit then reveals the ratio between the two rates, see also Fig. 6.2. The resulting ratio is 7.8 ± 0.7, following basic error propagation for $f = a_2/a_1$; indicating that the decrease in rate of movement for voltage scales faster than linearly.

The performance of the linear cryo-walkers seems excellent at RT, even at low voltages. It should most certainly be good enough to be part of the next cold run in the cryostat. This view was confirmed even more during tests at RT before the subsequent cold run. Before this run, there was enough time to perform a proper approach at (V_{lift}, V_{shear}) = (30 V, 64 V). The results are shown in Fig. 6.3. The behavior that is observed is exactly as expected, with the tip holder-sample capacitance dominating at larger distances, and a contribution of the tip-sample capacitance being clearly visible close by the sample.

6.2 Results after Cooldown

After the cooldown for this run of the *Marshmallow* had concluded, the MC-plate reached a final temperature of $T_{MC} \approx 70$ mK. Due to other experiments also being present and connected to the MC-plate, this temperature can go up to about $T_{MC} \approx 100$ mK.

6.2.1 Approaches

With the MC-plate having been cooled down to <100 mK, the Basic STM is ready to perform measurements with. A retraction was attempted first, at (V_{lift}, V_{shear}) = (150 V, 300 V). The capacitive readout seemed to show that the tip was moving, following the expected curve. After 75 steps of retraction, the approach was initiated. As the tip moved quicker than expected, it was chosen to immediately perform a fine approach until *CAMERA* measured a voltage higher than the setpoint (tunneling current or crash). This approach took a total of 178 steps.

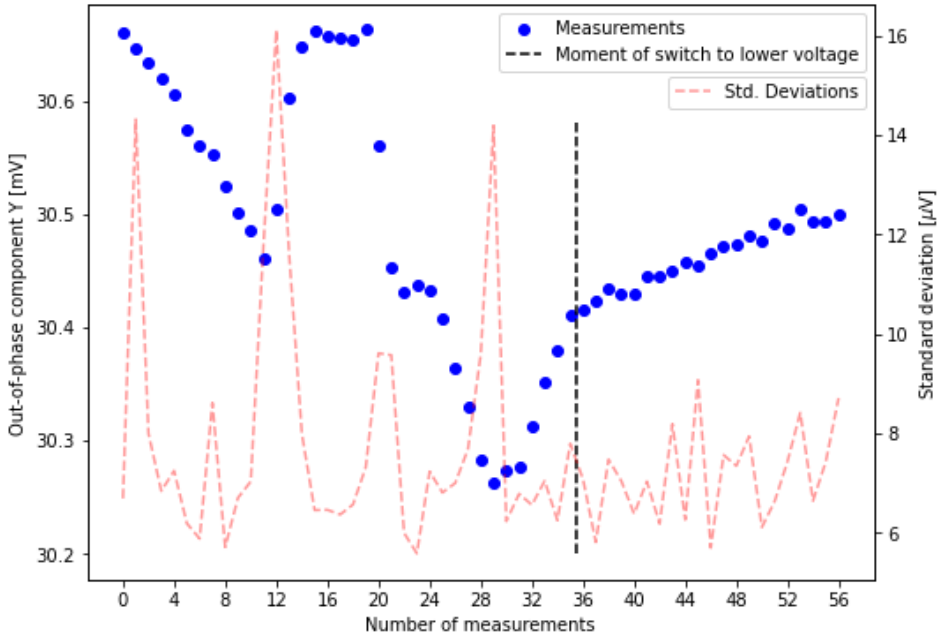

Figure 6.1: *Out-of-phase component Y measurements after the Basic STM was placed in the Marshmallow.*

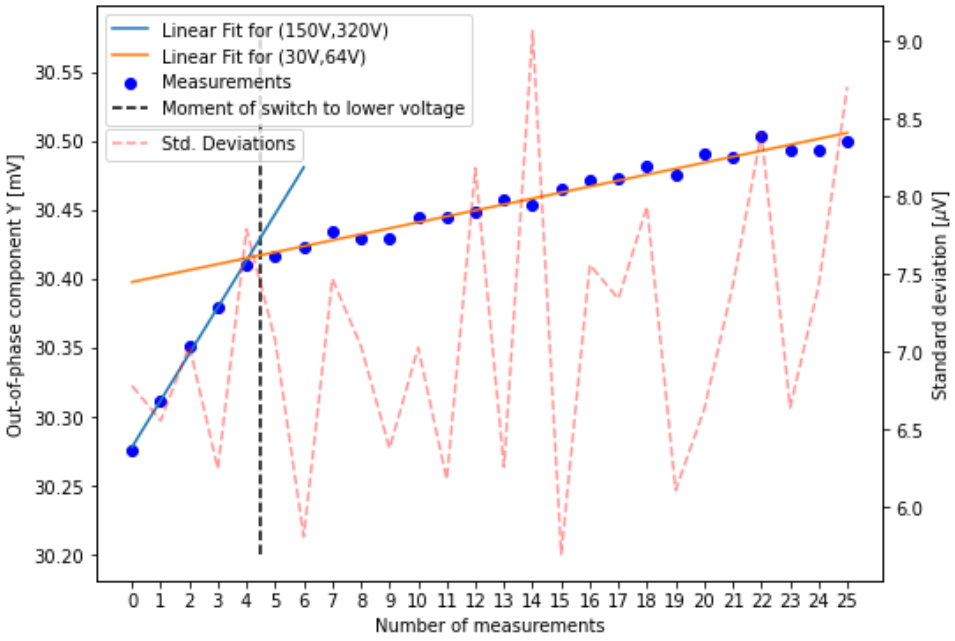

Figure 6.2: *Final approach with the Basic STM at RT in the cryostat, accompanied by two linear fits performed for the two different sets of voltages.*

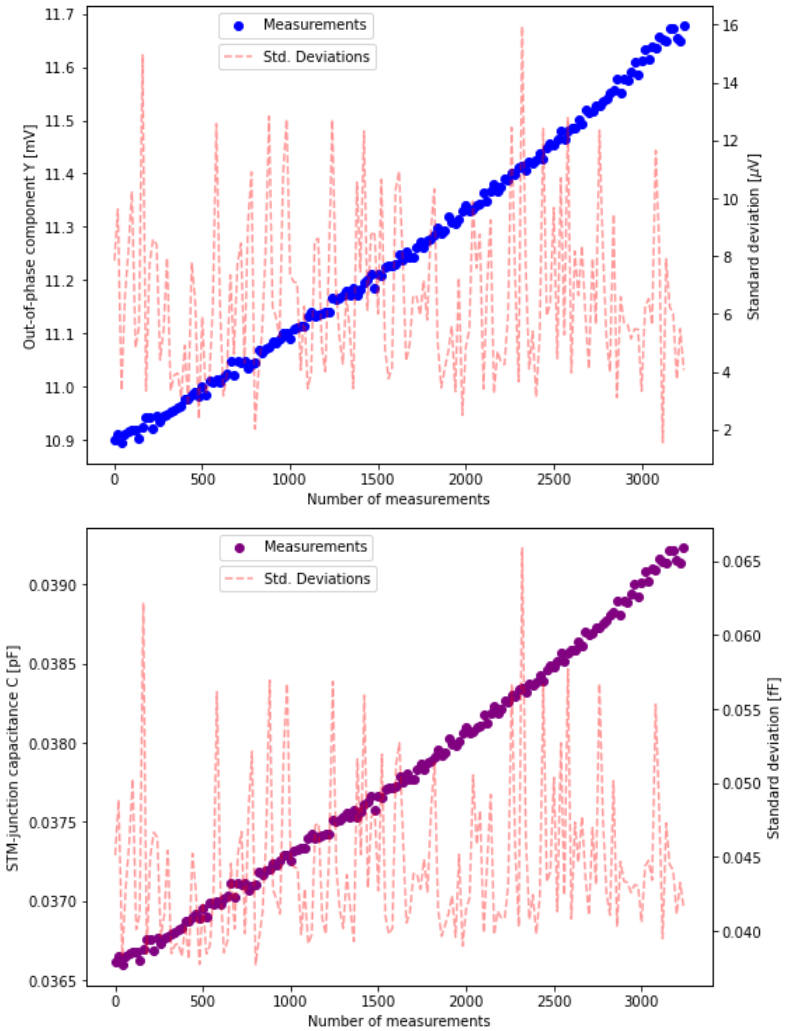

Figure 6.3: *Approach at RT before the subsequent cold run took place. The measurements were performed at a fifth of the maximal voltage.*

This process was repeated four consecutive times later that afternoon, to see the consistency of the movement. The amount of steps used can be seen in Table 6.1, and the measurements can be seen in Fig. 6.4a-d, where the out-of-phase component is again converted to an absolute capacitance via Eq. 2.6. Fig. 6.4e-f show the average taken over the four final, consecutive measurements. The first approach is not brought into this average, as the starting position seemed to differ much from the rest. This difference is most likely due to the fact that the first measurement was done way earlier, implying that there is a drift, or that some kind of mechanical vibration might have led to a slight shift in position.

The rate by which the tip seemed to retract and approach is very consistent, and is considerably fast when compared to the measurements at RT: over 180 steps, a rise of 0.5 mV is detected, while at RT, at (V_{shear}, V_{lift}) = (30 V, 64 V), a rise of 0.15 mV is detected after 35 steps. It therefore seems as if the capacitance of the piezos of the linear cryo-walker have decreased by less than a factor of 5. The retraction showed the same consistent behavior that has shown before, clearly following the expected behavior for a capacitive approach. The approach on the other hand, does seem to show some deviation from the expected curve. At the start of the approach, the capacitance rose quicker than expected, but flattened out a little to return to the expected behavior..

	1	2	3	4	5
Retract	75	75	75	75	75
Approach	178	180	180	184	178

Table 6.1: *Amount of steps taken to retract and re-approach for five measurements. The amount of steps for the retraction was equal on purpose, chosen for no particular reason; the amount of steps for the approach was the amount necessary to reach the voltage setpoint in CAMERA.*

6.2.2 Scan at 70 mK

All 5 times, the approach was stopped because of a tunneling current being sensed. Manually performed senses showed currents of the order 9.8 nA / 9.9 nA, indicating an overload, suggesting that the tip crashed into the sample and was unable to measure a tunneling current. A suspicion was that this result could be due to the walkers standing somewhat skew, or a flake of HOPG being stuck on the sample. If the latter were the problem, it could be fixed by sending a 10 ms pulse of 1 V onto the tip, which

can help with getting such a flake off the tip. Afterwards, a retraction was performed, followed by a few large shear steps parallel to the sample, to prevent that this flake could get picked up again during an approach. By making these shear steps, the possibility arises that the first of the two mentioned problems could accidentally be solved.

After a new approach, a tunneling current seemed to be found. Manual senses sometimes still led to an overload, but a tunneling current was measured about 3/4th of the time. Therefore, feedback was turned on and a scan was started. The relevant parameters were $V_{set} = 3.88$ V, $P = -28.2$ dB, $I = 7.33$ Hz, and f_{LPF} = 997 Hz. The scans were, again, too noisy.

An explanation for the noisy scans could be that the tip has most likely crashed a lot during the first attempts at an approach. A large amount of crashes would have caused the tip to be blunt and/or crooked, resulting in a lower spatial resolution and introducing less consistent results. This problem can be resolved in future cold runs by inserting a new tip into the tip holder of the STM. Another reason for the noisy scans could be the mechanical vibrations from the pulse tube. This can however not be confirmed until measurements have been performed with a new tip that is not damaged through crashing.

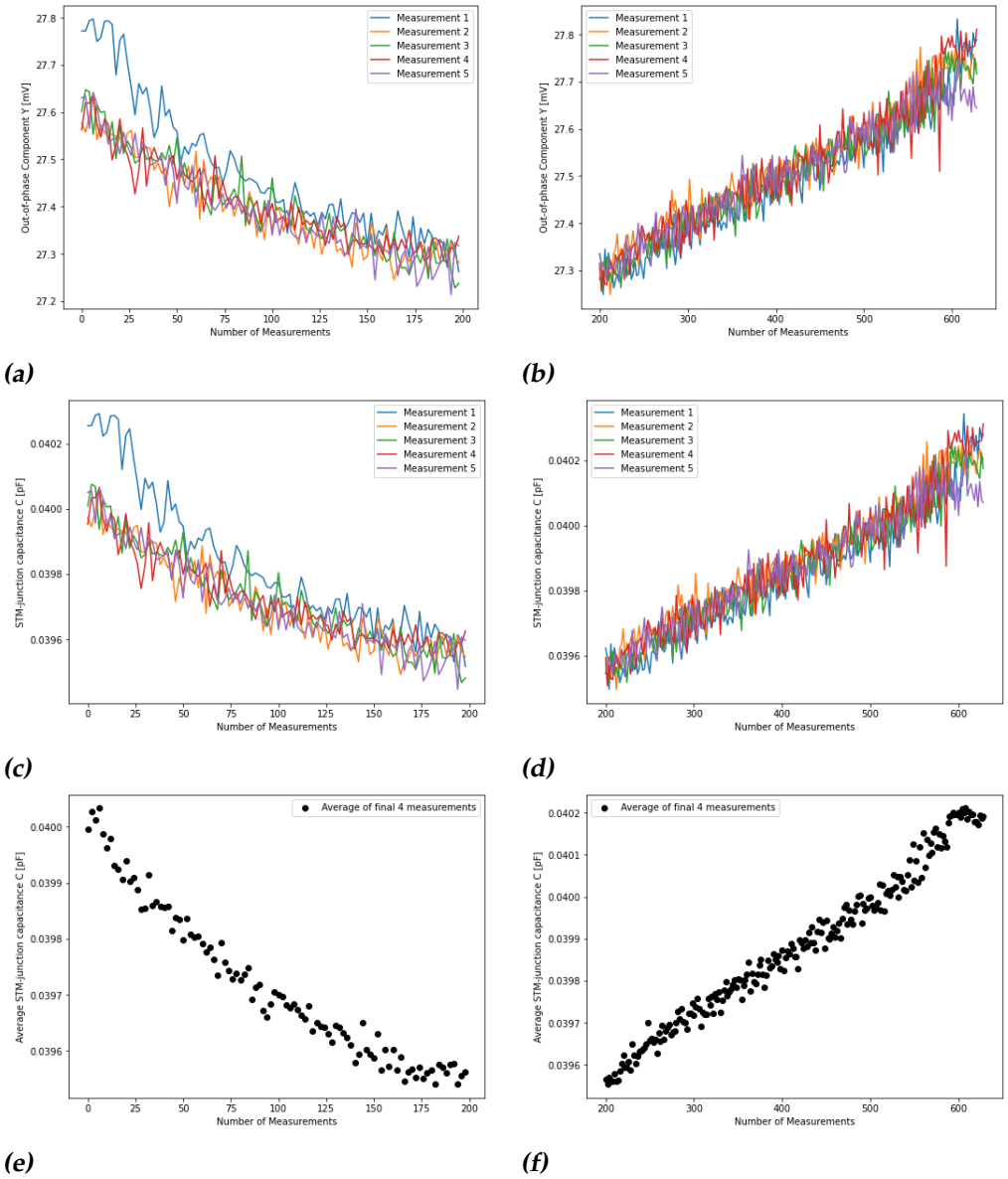

Figure 6.4: *Display of the capacitive readout for the retraction and approach with the Basic STM at 100 mK; (a-b) Out-of-phase component Y, (c-d) Y converted to an absolute capacitance C and (e-f) The absolute capacitance for the average, taken over the final 4 measurements..*

Chapter 7

Multi-LC

Superconductors are still a very active topic of research. Bardeen-Cooper-Schrieffer (BCS) theory, postulated in 1957, is currently the best attempt at a theoretical understanding of superconductivity [48]. It follows from BCS-theory that electrons can get bound into 'Cooper pairs' that would be the main cause of the superconductive properties that are observed in experiments. This bounding implies that the main charge carrier in a superconductive medium no longer has charge $q_e = e$, but $q_{CP} = 2e$, which will cause the shot noise level to increase. If a device can be made that is sensitive enough to be able to distinctly measure the shot noise, it would theoretically be possible to directly show the presence of Cooper pairs.

At temperatures of $T \sim 4$ K, shot noise measurements have already been achieved by Bastiaans et al. in the Allen lab at Leiden University [7]. An amplifier was created by use of an High-Electron Mobility Transistor (HEMT) and where necessary, parts of the setup were placed in a 4 K He-bath.

If one strives to do these shot noise measurements at temperatures of the order $T \sim 20$ mK , a HEMT could no longer be used [49]. A posed alternative is the 'Multi-LC circuit' (See Fig. 7.1). This circuit is especially designed for use in STM as a possible method of measuring shot noise in these extremely low temperature environments. It uses a SQUID, a superconducting quantum interference device, that can effectively be used as an amplifier at sub-kelvin temperatures. It has yet to be implemented in a circuit containing an STM, but progress has been made towards the analysis, showing an exciting prospect.

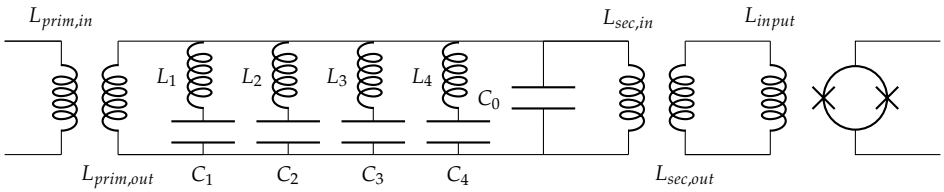

Figure 7.1: *Schematic of the Multi-LC circuit. From left to right: the circuit starts with a primary transformer to transfer electric energy towards the LC-resonators that make up the Multi-LC. The inductor of the primary resonator is electrically linked to the SQUID on the right via the second transformer. This way, the LC-resonators are fully modular.*

7.1 Theory

To understand how the Multi-LC circuit can be used, some theory needs to be presented. The topics to be discussed are the components of the circuit, some theory on the analysis of the noise spectra, and a mention of the relevant noise sources.

The components of the Multi-LC circuit can be divided up into 3 parts: the LC-resonators, the transformer and the SQUID. These components shall be discussed one by one, accompanied by formulae describing what is measured and how to convert them from one part to another.

7.1.1 LC-resonators

The Multi-LC circuit relies on having alternating resonances and anti-resonances. The theoretical foundation for such a circuit is described by Foster's reactance theorem [50]. Foster postulates that a circuit containing such alternating (anti-)resonances has the following complex impedance:

$$Z = -iH\frac{(\omega_1^2-\omega^2)(\omega_3^2-\omega^2)\dots(\omega_{2n-1}^2-\omega^2)}{\omega(\omega_2^2-\omega^2)\dots(\omega_{2n-2}^2-\omega^2)} \tag{7.1}$$

where $H \geq 0$ and with (anti-)resonance frequencies $0 = \omega_0 \leq \omega_1 \leq \cdots \leq \omega_{2n-1} \leq \omega_{2n} = \infty$. It clearly follows from this formula that the complex impedance will have zeroes at odd integer resonance frequencies, and poles for even integers. H defines the complex impedance at $\omega \gg \omega_{2n-1}$, as

$$\lim_{\omega\to\infty} Z(\omega) = -iH\frac{-\omega^2}{\omega} = iH\omega \tag{7.2}$$

Version of July 7, 2023– Created July 7, 2023 - 11:30

by which can be seen that H has units of inductance (units of impedance per Hz).

In the Multi-LC circuit, resonance frequencies are provided via LC-resonators. The complex impedance of a capacitor and inductor are, respectively:

$$Z_C = 1/i\omega C \qquad \text{and} \qquad Z_L = i\omega L \tag{7.3}$$

When an inductor and capacitor are placed in parallel, their impedances can be added reciprocally:

$$Z_{LC} = \frac{1}{1/Z_L + 1/Z_C} = \frac{i\omega L}{1 - (\omega/\omega_r)^2} \tag{7.4}$$

with $\omega_r = 1/\sqrt{LC}$ the resonance frequency.

Looking at the behavior of such a peak (see Fig. 7.2), it can be observed that the magnitude of the impedance increases until it reaches a pole at ω_r, after which the impedance shall decrease towards 0. In other words, a resonance is always enclosed in between two anti-resonances. With four LC-resonators placed in series, a pattern of alternating (anti-)resonances should emerge. This behavior is also confirmed through simulations in MicroCap.

Due to the concept of duality in electrical circuitry (including parallel $\leftrightarrow$ series, and capacitor $\leftrightarrow$ inductor) [51], having four LC-resonators placed in series is equivalent to having 4 sets of a capacitor and inductor in series, placed in parallel to one another. This is why the final circuit diagram of the Multi-LC looks it does in Fig. 7.1.

How to apply Foster's reactance theorem to obtain proper values for the relevant inductances and capacitances can be found in the work by van Deelen [51]. The relevant parameters for this project are $L_{sec,in} = 79\ \mu H$ and $L_{sec,out} = 2\ \mu H$. As the resonance frequencies only depend on the chosen capacitances and inductances, they could be chosen to be in the MHz-regime, where there should be little to no 1/f- and mechanical noise. If the entire circuit works as intended, the dominant noise sources that are left should only be thermal noise, and shot noise if an an STM is connected to the circuit.

The idea is that no current will run through these LC-components at the anti-resonances, causing all current to flow through the 'primary' LC-resonator. This should be the cause of resonance peaks in the noise spectrum of the circuit, occurring at the anti-resonance frequencies of the LC-resonators. Having multiple peaks should aid in doing a more accurate analysis. Considering the fact that thermal and shot noise are both types of white noise, all peaks should yield approximately equal results.

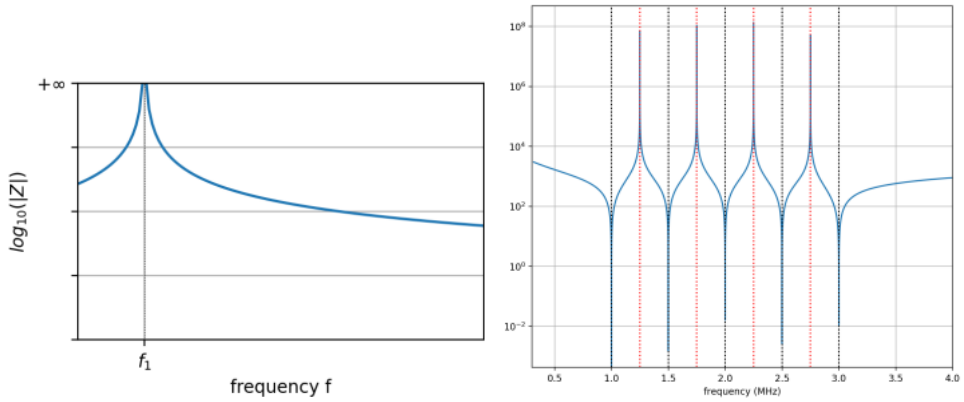

(a) *(b)*

Figure 7.2: *Plots of* $\log_{10}(|Z|)$ *for: (a) A single LC-resonator, and (b) An exemplary case of an impedance as described by Foster [51]. The impedance of Fig. b is purely theoretical, where the (anti-)resonances alternate every 0.25 MHz, in a bandwidth ranging from 1 MHz to 3 MHz.*

Since all current flows through the primary LC-resonator at resonance, it is expected that all energy under the resonance peaks is stored in the inductor belonging to said LC-resonator. With the current as presumably the only dominant degree of freedom, this would, via the equipartition theorem, imply that

$$\frac{1}{2}LI^2 = \frac{1}{2}k_B T_{eff} \qquad \text{or} \qquad T_{eff} = \frac{LI^2}{k_B} \tag{7.5}$$

where L is the inductance of the inductor, I the current current running through the LC-resonator at resonance, k_B the Boltzmann constant and T_{eff} an effective temperature. T_{eff} hypothetically is the temperature of the Multi-LC circuit, but would larger than this temperature in the presence of alternative energy sources, such as vibrational modes.

7.1.2 Transformer

A transformer is located in between the Multi-LC and SQUID. Due to the fact that the coil of the primary LC-resonator and the primary coil of the transformer have a different inductance, there is a conversion factor for the current on both sides of this junction. The relation for this factor can be derived for two ideal coils using Faraday's law of induction and energy conservation. There is also non-perfect coupling that needs to be taken

into account. This conversion factor, that will be called H_{tf}, is given by

$$H_{tf} = \kappa \cdot \sqrt{\frac{L_{sec,out}}{L_{sec,in}}} \qquad \text{such that} \qquad I_{LC} = H_{tf} \cdot I_{in} \tag{7.6}$$

where $\kappa \approx 0.5$ [51] is the coupling constant between the primary and secondary coil, and I_{in} the current through the input coil for the SQUID.

7.1.3 SQUID

The component on the right side of the circuit diagram in Fig. 7.1 is the SQUID, that is used to measure a signal originating from the LC-circuit. SQUID's are able to very sensitively measure magnetic flux. The flux in question, Φ_{in}, is induced by a current I_{in} on the input coil, which is the secondary coil of the transformer. These are related mutual inductance between the SQUID and the input coil.

$$\Phi_{in} = \frac{I_{in}}{1/M_{in}} \tag{7.7}$$

where $1/M_{in} = 0.21\mu A/\Phi_0$ [52] is the mutual inductance between the SQUID and input coil. Note that Φ_{in} is thus given as a multiple of the magnetic flux quantum $\Phi_0 = 2.1 \cdot 10^{-15}$ Tm^2.

A SQUID has to be tuned before each new use, by which is meant that some parts of its control need to be adjusted, such that it finds its 'working point'. To keep the SQUID at its working point for as long as possible, two types of feedback, negative and positive, with a custom feedback system can be attempted. Every time the SQUID is tuned, it changes the readout with the SQUID ever so slightly. Therefore, one needs to do a new calibration to obtain the correct conversion between the incoming flux and the measured voltage V_{SQ}. To do this conversion, there is the transfer coefficient V_Φ, that describes the slope of the V-Φ curve at the working point of the SQUID in units of V/Φ_0 (See 7.3). This coefficient can effectively be regarded as the voltage that is measured per incoming flux quantum. The transfer coefficient can be calculated with [52].

$$V_\Phi = \frac{dy}{dx} \cdot \frac{V_{period}}{m \cdot 2000} \tag{7.8}$$

where *dy/dx* is the slope at the working point in the V-Φ curve, in [V/V] units. V_{period} is the voltage per period as displayed on the interface. The

Version of July 7, 2023– Created July 7, 2023 - 11:30

factor 2000 and m originate from the amplification of *Amp*-mode, and magnification in the interface respectively. Using V_Φ, one is able to define the relation

$$V_{SQ} = V_\Phi \cdot \Phi_{in} \tag{7.9}$$

The SQUID also has a 'flux noise' of 1 $\mu\Phi_0$.

7.1.4 Noise Spectrum Analysis

Using equations 7.6-7.9, the conversion factor G is defined (units of conductance),

$$G \equiv \kappa \cdot \sqrt{\frac{L_{sec,out}}{L_{sec,in}}} \cdot \frac{1}{M_{in}} \cdot \frac{m \cdot 2000}{dy/dx \cdot V_{period}} \tag{7.10}$$

such that

$$I_{LC} = G \cdot V_{SQ} \qquad \text{and} \qquad S_I = G^2 \cdot S_V \tag{7.11}$$

to convert from a voltage to current power spectral density (PSD).

The resonance peaks of the Multi-LC will by approximation have the shape of a Lorentzian [53]. A function describing such a Lorentzian is of the form

$$S_I = A \cdot \frac{\Delta f}{(f - f_{res})^2 + \Delta f^2} \tag{7.12}$$

where A is a scale parameter, f_{res} the resonance frequency and Δf the half width at half maximum (HWHM). The quality factor Q is related to the other parameters via

$$Q = \frac{f_{res}}{2\Delta f} \tag{7.13}$$

If one wants to be able to make any claims on whether shot noise can be measured with the Multi-LC circuit, the signal-to-noise ratio (SNR) should be considered. For this experiment, (once an STM is actually connected to the Multi-LC and assuming that there is only thermal noise) the SNR is defined as:

$$SNR = \frac{P_{shot}}{P_{thermal}} = \frac{\sigma^2_{shot}}{\sigma^2_{thermal}} = \frac{S_{shot}}{S_{thermal}} \tag{7.14}$$

where S_{shot} and $S_{thermal}$ are the theoretical shot, and thermal noise current PSD. The final step in the derivation above holds because of both shot and thermal noise being types of white noise. To be able to measure the shot noise, an SNR greater than 1 is required. If the SNR is too small, one can perform multiple measurements to improve it, such that the noise is

averaged out. Doing N such measurements, improves the SNR by a factor $\sqrt{N}$.

Finally, it is relevant to calculate how much time it will take to do N measurements. Suppose a peak is well-defined with n data points. Then the time constant to obtain the required resolution for one measurement is

$$T = \frac{1}{f_{spacing}} = \frac{1}{2\Delta f / n} = \frac{nQ}{2f_{res}} \tag{7.15}$$

where $f_{spacing}$ is the difference in frequency between two data points. The total measurement time τ to achieve the required SNR_{req} becomes:

$$\tau \equiv N \cdot T = (\frac{SNR_{req}}{SNR})^2 \cdot \frac{nQ}{2f_{res}} \tag{7.16}$$

7.1.5 Noise Sources

Each electrical circuit will contain resistive components; albeit a resistor, wiring, etc. These components will deliver thermal noise, that results from the thermal agitation of charge carriers within an electrical conductor [54]. The voltage power spectral density (PSD) resulting from this component is

$$S_V = 4k_B TR \tag{7.17}$$

with k_B the Boltzmann constant, T the temperature of said component and R its resistance. This voltage PSD is in turn converted to a current PSD via Eq. 7.10.

Another type of noise that is usually considered for STM, is shot noise. An electric current is the result of many electrons, discrete packages of charge, flowing through the circuit. This will allow for statistical variations that get more noticeable, the lower the amount of electrons; this is observed as shot noise [54]. The caused current noise spectral density can be quantified as:

$$S_I = 2qI_0 \tag{7.18}$$

where I_0 is the average tunneling current and q the charge of the charge carriers. For an ordinary average tunneling current of 1 nA, this would imply a noise current of I_{RMS} = 17.9 fA/$\sqrt{\text{Hz}}$.

Other types of ordinarily dominant noise include 1/f-, 50Hz-noise and mechanical noise. Both 1/f- and 50Hz-noise can be avoided by working in the MHz-regime. Mechanical noise is expected to not be dominant, as the used cryostat has great vibration isolation [11, 12].

Version of July 7, 2023– Created July 7, 2023 - 11:30

7.2 Methods

The Multi-LC is placed on the MC-plate of the '*Yeti*' cryostat of the Oosterkamp Group. The *Yeti* is, just like the *Marshmallow*, a dry dilution refrigerator. A thermometer and heater are connected to the MC-plate, to be able to regulate and do measurements at different temperatures.

A Zürich Instruments HF2LI 50 MHz Lock-in Amplifier is used to obtain the noise spectra [55]. A lock-in uses AM-modulation and LPF's to allow for measurements in specific frequency slices, which makes it very suitable as a measurement device for this experiment. On the lock-in, a center frequency and bandwidth are chosen that determine the frequency slice along which is measured. The input impedance of this type of lock-in is 1 MΩ.

A choice can be made to either do a large sweep of an entire 1-6 MHz-spectrum or to look at a smaller slice, just around a resonance peak. Firstly, some large sweeps are done to locate the resonance peaks, by using a small input voltage from the lock-in. Subsequently, the peaks can be examined individually. Per peak, 5 measurements with a bandwidth of 50 kHz are done. A suspected resonance frequency is chosen as center frequency for the first measurement. The other measurements have a center frequency that is shifted by $\pm$5 kHz and $\pm$10 kHz with respect to the suspected center frequency. This action was taken as the lock-in always measures a little more signal at the center frequency, which can be considered to be an artifact. Afterwards, an average is performed over the 5 measurements to obtain a single voltage PSD. This should also significantly lower the contribution of the mentioned artifact.

Measurements were done at two separate temperatures. If it is observed during the analysis that the found values for T_{eff} do not comply with the expected temperatures of the circuit, having measurements at several temperatures can aid in understanding what is going wrong. For example, since the thermal voltage noise is proportional to temperature (Eq. 7.17), it should show linear behavior for increasing temperature.

7.3 Analysis

The starting point for the analysis is the voltage PSD acquired during measurements from the lock-in. Using Eq. 7.10, the voltage PSD can be converted to a current PSD. It is now possible to derive three quantities that are sought after.

The first one is the noise current that is amplified at the resonance

peaks. By dividing by the shape of the peak, one finds the level of the current noise. The shape of the peaks, a Lorentzian, can be found through a fit, by minimizing χ^2. The fit function is given by Eq. 7.12.

After dividing by the shape of the Lorentzian, a constant noise current PSD is found. By integrating over a given bandwidth Δf_I and dividing the resulting value by said bandwidth (and taking the square root), one finds the current noise root mean square (RMS) I_{RMS} [A/$\sqrt{\text{Hz}}$].

When the found value for I_{RMS} is greater than desired, multiple measurements can be performed to improve the SNR. The time that is consequently required to perform these measurements is given by Eq. 7.16.

The second quantity is an effective temperature. By integrating over a bandwidth Δf_T for the area under the peak, the energy stored in the inductor can be found. Subsequently, by using Eq. 7.5, a value for T_{eff} can be determined.

Finally, one can determine the usability of the circuit for shot noise measurements. Using Eq. 7.16, and the parameters found during earlier parts of the analysis, one can calculate the total measurement time that it takes to obtain an SNR of 1.

7.4 Results & Discussion

The first measurements were performed at an MC-plate temperature $T_1 \approx 100$ mK, whereas the second measurements were performed after the heater was used to heat up the MC-plate to $T_2 \approx 600$ mK. To make well-founded claims about temperature-related effects, measurements at more temperatures should have been performed. Alas, only these two measurements could be done due to a malfunctioning turbo-pump in the cryostat during the cold run. Measurements could have been performed at higher temperatures, but this would have been close to the regime in which the SQUID starts to give unreliable data.

7.4.1 Calibration

The first step in the analysis is to perform a calibration for both measurements. The used V/Φ-curves can be seen in Fig. 7.3.

T=100mK: The plot shows that $dy/dx = 1.75/0.44$ V/V, $V_{period} = 0.54$ V and $m = 10$. Using Eq. 7.10 and the other known parameters, a value for G is found: $G_1 = 1.56 \cdot 10^{-4}$ A/V.

T=600mK: The plot shows that $dy/dx = 1.675/0.37$ V/V, $V_{period} = 0.47$ V and $m = 10$. Using Eq. 7.10 and the other known parameters, a value

Version of July 7, 2023– Created July 7, 2023 - 11:30

for G is found: $G_2 = 1.57 \cdot 10^{-4}$ A/V.

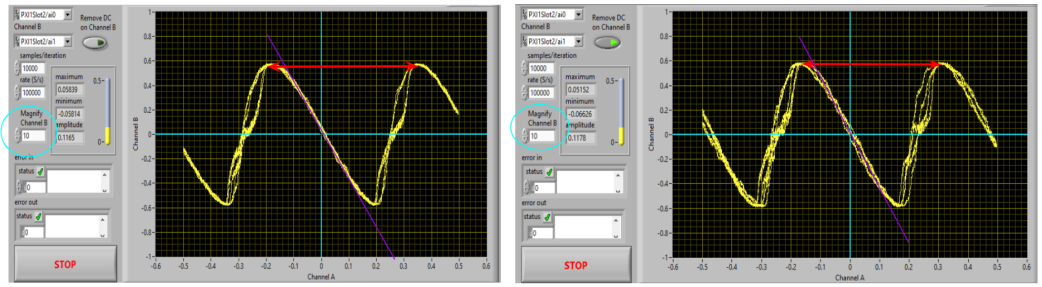

(a) ***(b)***

Figure 7.3: *V/Φ-curves of the SQUID for the performed measurements (left: 100 mK - right: 600 mK). The red line indicates V_{period}, the purple line indicates the slope dy/dx and the teal circle shows the interface magnification m.*

7.4.2 Spectrum Sweeps

Two kinds of large spectrum sweeps were performed. First (at 100 mK), a larger sweep is performed at different types of feedback and input voltages, see Fig. 7.4a. Four resonance peaks can be detected; two more peaks only occur for positive feedback. These peaks are most likely not resonance peaks of the LC-circuit, considering the fact that no phase shift is detected. The peaks most likely originate from the positive feedback itself. The other four peaks that are observed seem to occur in all three measurements, and all have a phase shift, indicating that these are most likely the resonance peaks that are sought for. The first peak is somewhat different from the rest, seemingly having a higher maximum and a smaller Q-factor with respect to the other peaks. It will be taken into the analysis regardless, to examine it further.

The second sweep was a little more zoomed in, ranging from 2MHz to 4.5 MHz, see Fig. 7.4b. The primary goal of this sweep was to see the spectrum that is predicted by Foster, as can be seen in Fig. 7.2b. By choosing a high input voltage (1 mV), the noise is negligible, and the expected spectrum starts to take shape (green curve). This measurement also shows a few extra peaks for positive feedback, that will be attributed to the feedback itself.

Subsequently, the measurements for individual peaks are done, as described by the Methods section. The raw data for one of the peaks is shown in Fig. 7.5.

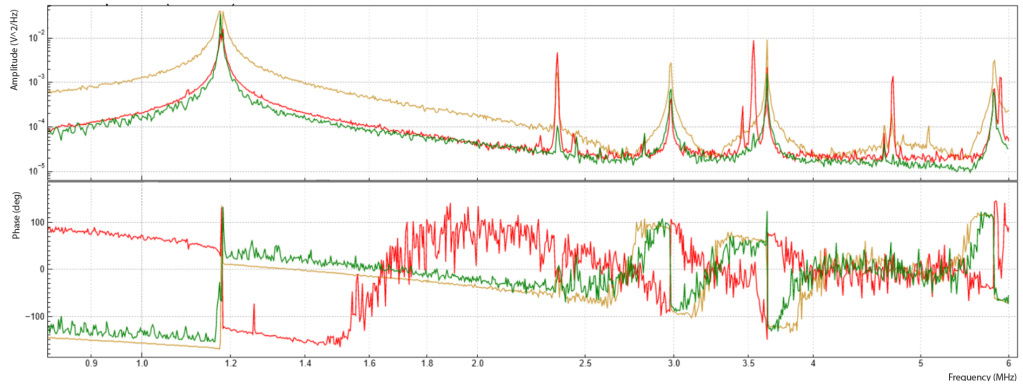

(a)

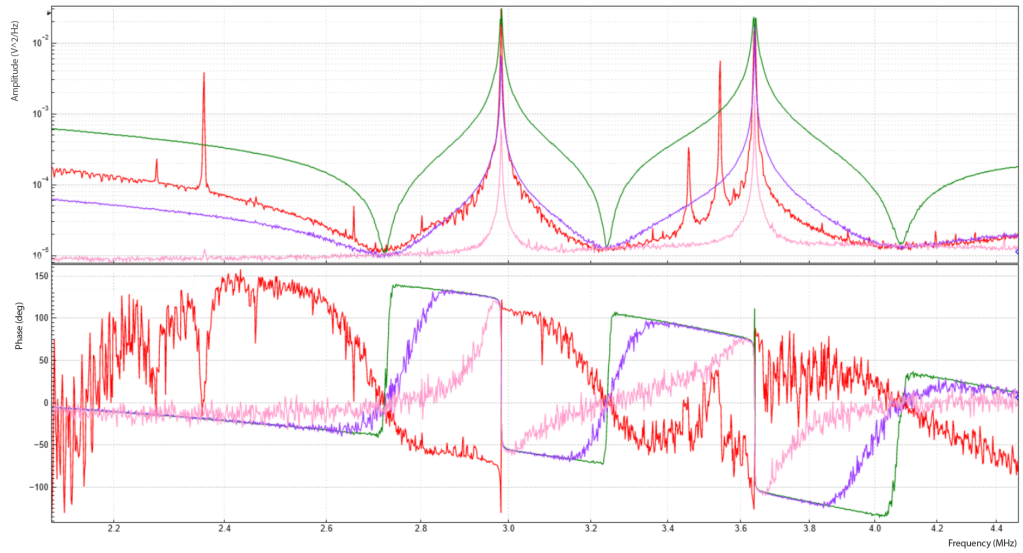

(b)

Figure 7.4: *(a) gold: no feedback, red: pos. feedback, green: neg. feedback (all at 100 µV). (b) green: neg. feedback at 1 mV, purple: neg. feedback at 100 µV, pink: neg. feedback at 10 µV, red: pos. feedback at 1 mV*

7.4.3 Resonance Peak Analysis

With the found values for G_1 and G_2, it will now be possible to carry out the rest of the analysis. Using a Python script, the analysis is carried out following the Analysis section. This yielded the results that are shown in table 7.1.

Following Eq. 7.17, the thermal voltage noise should be proportional to temperature. Therefore, if the found I_{RMS} values are only of a thermal nature, their squares should all show linear behavior as a function of tem-

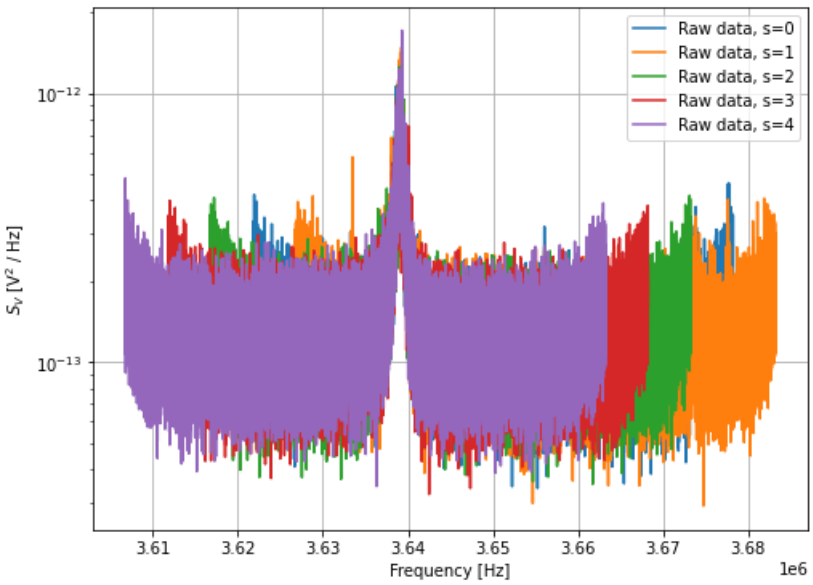

Figure 7.5: *Raw data for the 3rd resonance peak during the measurements at 100 mK. s indicates which measurement a given color depicts.*

perature. Hence,

$$\frac{\sigma_{T_2}^2}{\sigma_{T_1}^2} = \frac{T_2}{T_1} = \frac{600\text{ mK}}{100\text{ mK}} \tag{7.19}$$

The results of this are plotted in Fig. 7.6. It should be noted that in the presence of an extra noise source that is independent of temperature, this proportion is smaller. After all

$$\frac{\sigma_{T_2}^2 + C}{\sigma_{T_1}^2 + C} < \frac{\sigma_{T_2}^2}{\sigma_{T_1}^2} \tag{7.20}$$

for $C > 0$, which has to hold for the mentioned case.

The found thermal RMS currents are still relatively high when compared to that of shot noise, differing by a factor $\sim$100 for the 'best' peaks. Say the best peak, judging by lowest theoretical SNR, was chosen to perform shot noise measurements. The SNR follows from Eq. 7.18 and 7.14, with $I_0 = 1\text{ nA}/\sqrt{\text{Hz}}$ and $q = e$, and the square of I_{RMS} taken as the thermal current PSD. The best peak would then be the fourth peak (at $f_r = 5.82$ MHz) at 100 mK, with

$$SNR = \frac{2qI_0}{I_{RMS}^2} = \frac{320\text{ fA}^2/\text{ Hz}}{3.69\text{ pA}^2/\text{ Hz}} = 8.67 \cdot 10^{-5}$$

T	100mK				600mK			
	1	2	3	4	1	2	3	4
f_r [MHz]	1.18	2.98	3.64	5.82	1.18	2.98	3.64	5.82
Q	1313	2984	3494	3085	1165	9384	3193	2992
I_{RMS} [pA/$\sqrt{\text{Hz}}$]	12.9	3.99	2.01	1.92	26.9	12.6	5.88	2.34
T_{eff} [K]	1684	309	158	151	6769	3867	1079	279

Table 7.1: *Results from the resonance peak analysis of two measurements with the Multi-LC. From top to bottom: resonance frequency f_r and Q-factor Q of the resonance peak, RMS noise current I_{RMS} and effective temperature T_{eff}.*

Subsequently, assuming that a resonance peak is defined well enough for $n = 10$ data points, taking the Q-factor $Q = 3085$ of the peak, to find via Eq. 7.15 that the time constant for 1 measurement is $T = 2.65$ ms. To then achieve an SNR of 1, according to Eq. 7.16, the required total measurement time would have to approximately be $\tau \approx 98$ hours.

7.4.4 Discussion

The Q-factors, apart from one peak, seem to be consistent. At the two different temperatures, the Q-factor remains approximately the same, which should be expected for as low of a temperature rise as 0.5 K. The Q-factor of the second peak at 600 mK is abnormally high, which brings the validity of this measurement into question. The Q-factor seems to also be somewhat consistent over the peaks of the highest three measurements, with the first peak having a much lower Q-factor. Something that has been suspected, and wondered about, is whether the resonance at 1.18 MHz is the resonance frequency of the primary resonator. Its behavior seems to differ much from that of the other three peaks, indicating that the other three are most likely really from the LC-resonators, resulting in the conclusion that there might be another resonance peak that was not detected during the spectrum sweeps. This could be due to human error or due to a faulty element in the circuit.

It is difficult to make claims on the nature of the found I_{RMS}: due to the fact that there are measurements at only two temperatures, all claims that are made are non-conclusive. If the four data points were to be trusted, two argue in favor of an extra noise source, whereas the other two are only possible in the case of another temperature-dependent noise source. Possible sources of noise could be thermal noise from the lock-in that is at RT ($S_V = 1.61 \cdot 10^{-14}$ V^2/Hz), or the flux noise of the SQUID ($I_{LC,SQUID} =$

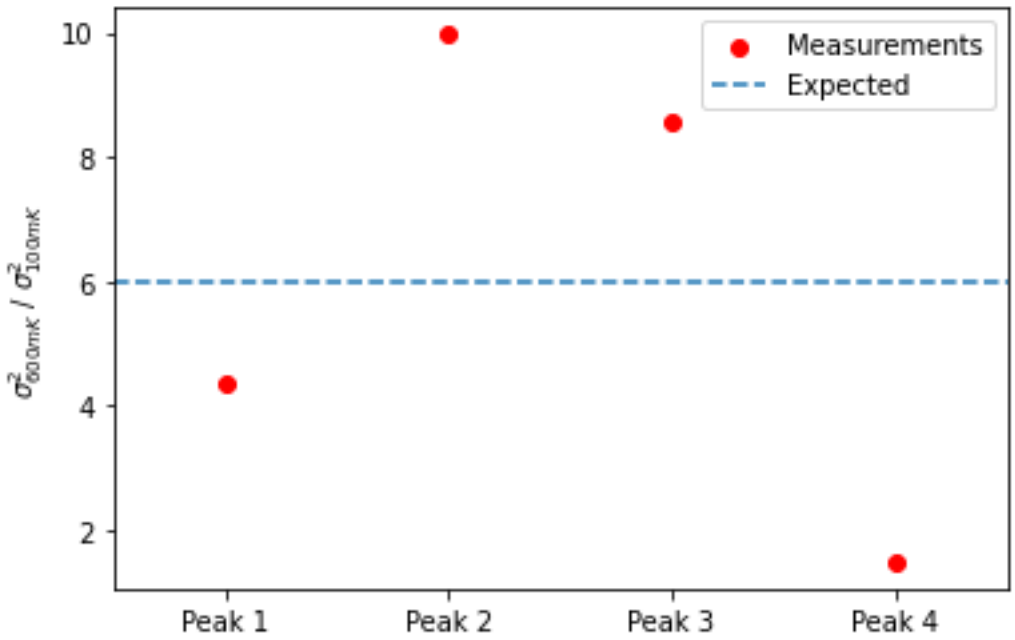

Figure 7.6: *Determination of the ratio between the voltage noise at 100 mK and 600 mK. When the measurements are trusted, all peaks should lay underneath the dotted line.*

16.7 fA/$\sqrt{\text{Hz}}$). These both do not seem to be sufficiently large.

The nature of T_{eff} should also be brought into question. The found values for T_{eff} do not agree with the temperatures of the MC-plate at the time of measurement. With the question on whether all noise is of a thermal nature being unanswered, this is not an illogical result. However, the validity of the calculations for T_{eff} is also still under investigation. For example: is it correct to choose the inductance L of the primary LC-resonator or should the other inductances also be taken into account? Is any energy stored in the capacitor of the LC-resonator? More experiments need to be performed to answer these questions.

Currently, the assumption has been made that $n = 10$, is a sufficient amount of data points to recognize a Lorentzian in a resonance peak well enough. A more precise number for n is something that should be looked into to ensure more accurate predictions on a total measurement time. This could be done by running simulations/fits on sliced data sets. If one defines an accuracy to which extent the fit has to comply, one can determine a more precise value for n.

The total time for one measurement with an SNR of 1 was approxi-

mately 100 hours. This result touches on why dry dilution refrigerator STM can be so important. With an STM in a wet dilution refrigerator, measurements that take 100 hours are not realistic. In a dry dilution refrigerator however, this is something that could theoretically be done. The Multi-LC circuit might not be the best example, since it has shown its shortcomings and needs some more close examination, there are definitely experiments out there that can really benefit from such long measurement times (or even longer) at cryogenic temperatures.

Chapter 8

Conclusion

The main goal for this project was to test the performance of the motors of the two STM's at cryogenic temperatures. The linear cryo-walkers from Onnes Technologies have shown to be able to perform a complete approach and a scan at sub-kelvin temperatures, resulting in very low heat dissipation. The STM showed great prowess and the prospect of a new cold run with an undamaged tip is exciting, hopefully resulting in atomic resolution scans. The Basic STM seems like a great option for dry dilution refrigerator STM.

The PH-STM has not shown equally good results. The PAN-motor showed less motion at RT already with regards to the cryo-walkers, and seems to have fully malfunctioned during the cooldown of the *Marshmallow*. The slip-stick piezos have shown to produce large amounts of heat, which speaks against using the configuration to do a coarse approach at temperatures under 4 K. A recommendation would be to try creating a design in which the cryo-walkers could be integrated into the PH-STM. This way, the PH-STM could be used in the future in combination with the proposed elevator system for in operando tip exchange and sample preparation.

The developed analysis for the Multi-LC has shown that the circuit is usable to some extent. Some doubt can can be cast over some of the measurements, so the validity of the result needs to be reconsidered. Performing new measurements in a new cold run of *Yeti* would be recommended. Meanwhile, a single measurement with large enough SNR would require approximately four days of continuous measuring, as $\tau \approx 98$ h. This is a large amount, but not infeasible. It should also be noted that the measurements and analysis have been done with the first, non-optimized version of the circuit, implying that the total measuring time can only be improved

upon. The long amount of time does however emphasize why dry dilution refrigerator STM can be so useful, as multiple four days long measurements would not be feasible in a wet dilution refrigerator.

8.1 Acknowledgments

The BRP has been more fun than I could have ever wished for. 17-year old me would not have believed it, but I have secretly fallen in love with experimental research. I hope that I will continue to have as much fun with research as I have in the past 4 months.

I would like to start by thanking Tjerk, for allowing me to conduct research in his amazing research group, and with the *Yeti* and *Marshmallow*. Your passion for research has truly inspired me to become the best researcher I can be.

Koen, you were the best and nicest daily supervisor I could have hoped for; I really enjoyed all of our daily chats and laughter. Thank you for taking me under your wing and teaching me so much about experimental research. I hope that I can one day read and learn about your successes with the STM's and the Multi-LC.

David, thanks for all of your help with the STM's whenever we did not see the light at the end of the tunnel anymore. Your 'hacky' way of doing research has really taught me to think in another way about research. Enjoy your future life as a dad :).

Thanks also go out to Merlijn (FMD), and Raymond (ELD), for their ability to create everything that we needed for our experiments. Norman, thank you for teaching Koen and me how to use the etching station of the van Ruitenbeek Group. Professor van Ruitenbeek, thank you as well for willing to be my second reader.

I really want to thank my fellow BRP students in the Oosterkamp Group as well: Oscar, Reinier and Timo. I really enjoyed our little holiday in Germany, all of our coffee/choco-crème/'Oscar Special' breaks, and having you as friends in general. I hope that I will stay close to all three of you, so that I can see you prosper in your future careers. I am certain that you will.

Finally, I would like to mention the other members of the Oosterkamp Group: Tim, Jaimy, Dennis, Lars and Sanaz, you all contributed to a really pleasant atmosphere in the Oude Meethal and Nieuwe Meethal, for which I am very grateful. The same holds for the Hensen Group members; Bas, Martijn, Stef and Aaron.

Fin.

Bibliography

[1] G. Binnig and H. Rohrer, *Scanning tunneling microscopy*, Surface Science **126**, 236:244 (1983).

[2] NobelPrize.org, *The Nobel Prize in Physics 1986 [Press Release].*, (1986, October 15), Retrieved June 6th, 2023.

[3] A. Zhao, S. Tan, B. Li, B. Wang, J. Yang, and J. G. Hou, *STM tip-assisted single molecule chemistry*, Physical Chemistry Chemical Physics **15**, 12428:12441 (2013).

[4] J. A. Zasadzinski, *Scanning tunneling microscopy with applications to biological surfaces*, Biotechniques **7**, 174:187 (1989).

[5] M. T. Randeria, B. E. Feldman, I. K. Drozdov, and A. Yazdani, *Scanning Josephson spectroscopy on the atomic scale*, Physical Review B **93** (2016).

[6] J. Lawrence, G. C. Sosso, L. Đorđević, H. Pinfold, D. Bonifazi, and G. Constantini, *Combining high-resolution scanning tunneling microscopy and first-principles simulations to identify halogen bonding*, Nature Communications **11** (2020).

[7] K. M. Bastiaans, D. Cho, D. Chatzopoulos, M. Leeuwenhoek, C. Koks, and M. P. Allan, *Imaging doubled shot noise in a Josephson scanning tunneling microscope*, Phys. Rev. B **100**, 104506 (2019).

[8] L. Wang, Y. Xia, and W. Ho, *Atomic-scale quantum sensing based on the ultrafast coherence of an H_2 molecule in an STM cavity*, Science **376**, 401:405 (2022).

[9] T. Balashov, M. Meyer, and W. Wulfhekel, *A compact ultrahigh vacuum scanning tunneling microscope with dilution refrigeration*, Review of Scientific Instruments **89** (2018).

[10] Y. J. Song, A. F. Otte, V. Shvarts, Z. Zhao, Y. Kuk, S. R. Blankenship, A. Band, F. M. Hess, and J. A. Stroscio, *Invited Review Article: A 10 mK scanning probe microscopy facility*, Review of Scientific Instruments **81** (2010).

[11] A. M. J. den Haan, G. H. C. J. Wijts, F. Galli, O. Usenko, G. J. C. van Baarle, D. J. Zalm, and T. H. Oosterkamp, *Atomic resolution scanning tunneling microscopy in a cryogen free dilution refrigerator at 15 mK*, Review of Scientific Instruments **85** (2014).

[12] T. M. Fuchs, D. Uitenbroek, J. Plugge, N. van Halteren, A. Vinante, H. Ulbricht, and T. H. Oosterkamp, *Magnetic Zeppelin: Detection of gravitational drive in the Hz regime*, arXiv: quant-ph (2023).

[13] R. P. Aloysius, S. Husale, A. Kumar, F. Ahmad, A. K. Gangwar, G. S. Papanai, and A. Gupta, *Superconducting properties of tungsten nanowires fabricated using focussed ion beam technique*, Nanotechnology (2019).

[14] D. U. Gubser and R. J. Soulen, *Thermodynamic properties of superconducting iridium*, Journal of Low Temperature Physics , 211:226 (1973).

[15] J. M. de Voogd, M. A. van Spronsen, F. E. Kalff, B. Bryant, O. Ostijić, A. M. J. den Haan, I. M. N. Groot, T. H. Oosterkamp, A. F. Otte, and M. J. Rost, *Fast and reliable pre-approach for scanning probe microscopes based on tip-sample capacitance*, Ultramicroscopy **181**, 61:69 (2017).

[16] C. J. Chen, *Introduction to Scanning Tunneling Microscopy*, chapter 2, page 42:66, Oxford University Press, 2021.

[17] M. N. Huda, *Epitaxial growth of lateral graphene / hexagonal boron nitride heterostructures*, PhD thesis, Aalto University, Espoo, Finland, 2016.

[18] C. J. Chen, *Introduction to Scanning Tunneling Microscopy*, chapter 15, page 363:378, Oxford University Press, 2021.

[19] J. Tersoff and D. R. Hamann, *Theory and Application for the Scanning Tunneling Microscope*, Physics Review Letters , 1998:2001 (1983).

[20] J. Tersoff and D. R. Hamann, *Theory of the scanning tunneling microscope*, Physics Review B **31**, 805:813 (1985).

[21] A. H. Sørensen, U. Hvid, M. W. Mortensen, and K. A. Mørch, *Preparation of platinum/iridium scanning probe microscopy tips*, Review of Scientific Instruments **70**, 3059:3067 (1999).

[22] B. Li, Y. Zhang, J. Wang, Z. Jia, C. Shi, Y. Ma, and L. Ma, *Fabricating ultra-sharp tungsten STM tips with high yield: double-electrolyte etching method and machine learning*, SN Applied Sciences **1246** (2020).

[23] I. H. Musselman and P. E. Russell, *Platinum/iridium tips with controlled geometry for scanning tunneling microscopy*, Journal of Vacuum Science and Technology A **8** (1990).

[24] B. Ju, Y. Chen, and Y. Ge, *The art of electrochemical etching for preparing tungsten probes with controllable tip profile and characteristic parameters*, Review of Scientific Instruments **82** (2011).

[25] J. G. Rodrigo, H. Suderow, and S. Vieira, *On the use of STM superconducting tips at very low temperatures*, The European Physical Journal B **40**, 483:488 (2004).

[26] P. Richter, A. Beck, O. M. Froehlich, R. Gross, and G. Koren, *Conductance zero bias anomaly in high temperature superconducting grain boundary Josephson junctions*, Czechoslovak Journal of Physics **46**, 1303:1304 (1996).

[27] C. J. Chen, *Introduction to Scanning Tunneling Microscopy*, chapter 10, page 277:298, Oxford University Press, 2021.

[28] G. Martinet, S. Blivet, F. Chatelet, M. Fouaidy, N. Hammoudi, A. Olivier, and H. Saugnac, *Low Temperature Properties of Piezoelectric Actuators used in SRF Cavities Cold Tuning Systems*, EPAC 2006 - Contributions to the Proceedings (2006).

[29] P. B. Rasmussen, B. L. M. Hendriksen, H. Zeijlemaker, H. G. Ficke, and J. W. M. Frenken, *The Reactor STM: A scanning tunneling microscope for investigation of catalytic surfaces at semi-industrial reaction conditions*, Review of Scientific Instruments **69**, 3879:3884 (1998).

[30] M. Marz, G. Goll, and H. von Löhneysen, *A scanning tunneling microscope for a dilution refrigerator*, Review of Scientific Instruments **81** (2010).

[31] C. J. Chen, *Introduction to Scanning Tunneling Microscopy*, chapter 12, page 313:328, Oxford University Press, 2021.

[32] L. B. Wilner, *Variable Capacitance Liquid Level Sensors*, Review of Scientific Instruments **31**, 501:507 (1960).

[33] C. J. Chen, *Role of Tip Material in Scanning Tunneling Microscopy*, MRS Online Proceedings Library (OPL) **159**, 289 (1989).

[34] A. T. A. M. de Waele, *Basic Operation of Cryocoolers and Related Thermal Machines*, Journal of Low Temperature Physics **164**, 179:236 (2011).

[35] R. Q. Regter, *Spin Density Determination by means of Low Temperature Magnetic Resonance Force Microscopy*, Bachelor's Thesis, Leiden University, Leiden, the Netherlands, 2023.

[36] G. van Baarle and M. Moene, *Camera Application - Computer Aided Measurement Environment for Realtime Atomic imaging*, `https://secure.eld.leidenuniv.nl/~moene/software/camera/Camera/Camera-MainPage.html`. Retrieved on June 15th, 2023.

[37] O. El-Atwani, D. V. Quach, M. Efe, P. R. Cantwell, B. Heim, B. Schultz, E. A. Stach, J. R. Groza, and J. P. Allain, *Multimodal grain size distribution and high hardness in fine grained tungsten fabricated by spark plasma sintering*, Materials Science and Engineering: A **258**, 5670:6577 (2011).

[38] A. Revenikiotis, *Optimization of STM-tip preparation methods*, Master's thesis, Kungliga Tekniska HÃ¶gskolan, Stockholm, Sweden, 2010.

[39] A. Warren, A. Nylund, and I. Olefjord, *Oxidation of tungsten and tungsten carbide in dry and humid atmospheres*, International Journal of Refractory Metals and Hard Materials **14**, 345:353.

[40] M. Kuwabara, D. R. Clarke, and D. A. Smith, *Anomalous superperiodicity in scanning tunneling microscope images of graphite*, Applied Physics Letters **56**, 2396:2398 (1990).

[41] M. Ohler, J. Baruchel, A. W. Moore, P. Galez, and A. Freund, *Direct observation of mosaic blocks in highly oriented pyrolytic graphite*, Nuclear Instruments and Methods in Physics Research Section B: Beam Interactions with Materials and Atoms **129**, 257:260 (1997).

[42] Y. Yuan, W. Li, H. Chen, Z. Wang, X. Jin, and G. Z. Chen, *Electrolysis of metal oxides in MgCl2 based molten salts with an inert graphite anode*, Faraday Discussions **190**, 85:96 (2016).

[43] Stanford Research Instruments, Sunnyvale, California, USA, *MODEL SR830 DSP Lock-In Amplifier*, revision 2.5 edition, 1993.

[44] National Instruments Corporation, Austin, Texas, USA, *myDAQ Specifications*, 2023.

[45] Femto Messtechnik GmbH, Berlin, Germany, *Datasheet DLPCA-200 Variable Gain Low Noise Current Amplifier*, 2019.

[46] J. Kim, H. Nam, S. Qin, S.-u. Kim, A. Schroeder, D. Eom, and C.-K. Shih, *Compact low temperature scanning tunneling microscope with in-situ sample preparation capability*, Review of Scientific Instruments **86** (2015).

[47] M. Kouwenhoven, *Novel Cryogenic Nanopositioning Technique Progresses into the Quantum Sensing Decade*, Cryogenic Society of America: Cold Facts **39** (2023).

[48] J. Bardeen, L. N. Cooper, and J. R. Schrieffer, *Theory of Superconductivity*, Physical Review **108** (1957).

[49] E. Dogmus, R. Kabouche, S. Lepilliet, A. Linge, M. Zegaoui, H. Ben-Ammar, M.-P. Chauvat, P. Ruterana, P. Gamarra, C. Lacam, M. Tordjman, and F. Medjdoub, *InAlGaN/GaN HEMTs at Cryogenic Temperature*, Electronics **5** (2016).

[50] R. M. Foster, *A Reactance Theorem*, Bell System Technical Journal **3**, 259:268 (1924).

[51] K. van Deelen, *Multi-LC; Designing a Multi Resonator Circuit to Enable Multi-frequency Readout of STM Current Noise in the MHz Regime with a SQUID*, Master's thesis, Leiden University, Leiden, the Netherlands, 2021.

[52] MAGNICON GmbH, Hamburg, Germany, *High Performance dc SQUID Electronics - XXF-1 Manual*, 2012.

[53] I. S. Kuijf, *Towards LC SQUID thermometry: measuring sub-Kelvin temperatures with high frequency noise*, Bachelor's Thesis, Leiden University, Leiden, the Netherlands, 2021.

[54] P. Horowitz and W. Hill, *The Art of Electronics*, chapter 7.11, page 430:433, Cambridge University Press, 1980.

[55] Zürich Instruments AG, Zürich, Switzerland, *HF2 User Manual*, 2023.